FISFVIFR

Contents lists available at ScienceDirect

International Journal of Plasticity

journal homepage: www.elsevier.com/locate/ijplas





On adiabatic shear instability in impacts of micron-scale Al-6061 particles with sapphire and Al-6061 substrates

Qiyong Chen ^a, Wanting Xie ^{b,c}, Victor K. Champagne ^d, Aaron Nardi ^d, Jae-Hwang Lee ^b, Sinan Müftü ^{a,*}

- ^a Department of Mechanical and Industrial Engineering, Northeastern University, Boston, MA 02115, USA
- ^b Department of Mechanical and Industrial Engineering, University of Massachusetts, Amherst, MA 01002, USA
- ^c Department of Physics, University of Massachusetts, Amherst, MA 01002, USA
- ^d United States Army Research Laboratory, Aberdeen Proving Ground, Aberdeen, MD 21005, USA

ARTICLE INFO

Keywords: Cold spray Impact mechanics Ultra high strain rate Adiabatic shear instability Finite element simulation Bilinear Johnson-Cook model Cohesive zone model

ABSTRACT

Impact mechanics of micron-scale, Al-6061 particles on sapphire and Al-6061 substrates were investigated experimentally and through simulations. Particle impact experiments were carried out by using the laser induced projectile impact test (LIPIT) and the coefficient of restitution was evaluated for impact velocities in the range of 50-950 m/s. Bonding was observed only in Al-on-Al impacts with impact velocities over 810 m/s. A continuum model of the impacts was implemented by using commercially available finite element software. The bilinear Johnson-Cook model was implemented to model the material flow effects in the ultra-high strain rate (UHSR) regime. A cohesive zone model was used for the bonding along the particle-substrate contact interface. Heat generation due to plasticity and friction, and material damage were also included in the simulations. A quantitative measure of adiabatic shear instability (ASI) was implemented into the modeling framework to search for material points that experience drop of strength during loading. A small volume of the material internal to the particle was found to experience ASI in Al-on-sapphire impacts, but this was not observed in Al-on-Al impacts. However, if the flow rule is switched to one that neglects the effects of the UHSR-regime, ASI can be predicted in regions of the particle where the finite element mesh deforms excessively. It is recommended that any study searching for ASI in high-velocity impact simulations should assess the mesh distortion carefully and use a flow rule that includes UHSR effects.

1. Introduction

Cold gas dynamic spray, commonly known as cold spray (CS), is an additive manufacturing technology which permits solid state deposition of coatings and three-dimensional (3D) manufacturing of free form objects by using a wide group of materials (Moridi, 2017; Gartner, 2006; Fauchais et al., 2014; Bala et al., 2014; Moridi et al., 2014; Intrater, 2002; Villafuerte, 2005; Schmidt et al., 2009; Van Steenkiste et al., 1999). Cold spray was originally developed in the mid-1980s at the Institute of Theoretical and Applied Mechanics of the Russian Academy of Science in Novosibirsk by Papyrin et al. (2006). In the cold spray process, micron scale particles with diameters typically under $100 \mu m$ are accelerated in a supersonic gas stream to velocities of 400-1200 m/s (Champagne et al., 2007; Klinkov et al., 2005; Papyrin and Blose, 2003). The resulting impact lasts 20-40 ns and causes deformations with ultra high strain rates (UHSR) that reach 10^6 to 10^8 s⁻¹ where extreme physics of the material is expected (Meyers, 1994). Powder particles

E-mail address: s.muftu@northeastern.edu (S. Müftü).

^{*} Corresponding author.

bond to the substrate or existing layers of the deposition if the kinetic energy of impact, plastic dissipation and work of adhesion are in a range of favorable proportions.

The mechanism of bonding in cold spray deposition has attracted significant interest. It is widely acknowledged that a powder particle needs to reach a threshold velocity, commonly known as the critical velocity, to develop successful bond with the substrate or existing deposit (Champagne et al., 2007, 2005; Assadi et al., 2003; Grujicic et al., 2003, 2004). There are two major causes of bonding, namely metallic bonding along exposed clean metal surface (Assadi et al., 2003; Champagne et al., 2007; Grujicic et al., 2004) and mechanical interlocking (Champagne et al., 2005; Grujicic et al., 2003). Early simulation work showed that when a powder particle impacts the surface above the critical impact velocity, material near the contact interface forms jetting induced by adiabatic shear instability (ASI); the intense plastic deformation from jetting exposes the intact metal underneath the oxide layers and metallic bond is formed thereafter (Assadi et al., 2003; Grujicic et al., 2004). More recently a new explanation was proposed by Hassani-Gangaraj et al. (2018), Assadi et al. (2019), Hassani-Gangaraj et al. (2019) which states that the driving mechanism for jetting is the release of pressure/shock wave at the free surface on the periphery of contact interface, rather than ASI. This explanation was reinforced by coupled-Eulerian-Lagrangian (CEL) simulations of impact (Hassani-Gangaraj et al., 2018). The critical velocity for a pure metal was estimated to be proportional to the material's bulk speed of sound based upon the relationship between the shock wave's propagation speed and velocity of the moving edge of the interface. The critical velocity thus predicted was validated through experiments (Hassani-Gangaraj et al., 2018, 2019). Suresh et al. (2020) further validated this explanation with quasi-coarse-grained-dynamics (OCGD) simulation of single particle impacts at mesoscale. They reported that for impact of pure Al-on-Al the thermal boost-up zone for ASI was not observed while a temperature spike as well as the thermal softening effect were present immediately following jet initiation at about 5 ns. It was also emphasized that the time-scale for ASI is around tens of nanoseconds following impact while jetting usually occurs in a few nanoseconds following impact. This coincides with the pressure shock wave release (Hassani-Gangaraj et al., 2018; Suresh et al., 2020), further questioning the necessity and even existence of ASI in CS bonding process.

In cold spray particle impacts, severe plastic deformation occurs in a very short time. Lin et al. divided up the impact into three stages: initial shock, peening and bonding and cooling stages (Lin et al., 2019). Strain hardening, strain-rate hardening and thermal softening are the three dominating factors for flow stress behavior during these stages. Strain rates that are on the order of 10^6 - 10^8 s⁻¹ are common during the first 30 ns following impact (Xie et al., 2017; Chen et al., 2018; Chen, 2020). Careful treatment of the factors that influence the flow stress in this duration is essential to reveal the material and mechanistic mechanisms of high speed particle impacts.

Behavior in the high strain rate (HSR) regime (up to 10⁴ s⁻¹) has been investigated experimentally. Gray (2000), Kolsky (1949), Harding et al. (1960), Hauser (1966), Lindholm and Yeakley (1968), Rittel et al. (2002), Zhao et al. (1998), Huang et al. (2011), Zhao (2011), and theoretically (Armstrong and Zerilli, 1994; Gao and Zhang, 2012; Johnson and Cook, 1983; Khan and Liang, 1999, 2000; Preston et al., 2003; Voyiadjis and Abed, 2005). Numerical simulations are often used to reveal the extreme physics during cold spray particle impacts due to the difficulties of observing the impact process with experimental measures. Various numerical methods are suitable for simulation the impact process, such as pure Lagrangian finite element method (FEM), smooth-particle-hydrodynamics (SPH) and coupled-Eulerian–Lagrangian (CEL) method (Fardan et al., 2021). Though, CEL is superior in computational accuracy, Lagrangian FEM is still the most popular method in modeling impact process which involves bonding behavior because of its advantage in contact interface tracking and ease of analyzing the results.

There are several existing constitutive models suitable for HSR and elevated temperature scenarios. Among the broad array of physically based HSR material models are Zerilli–Armstrong (ZA) model (Armstrong and Zerilli, 1994), Preston–Tonks–Wallace (PTW) model (Preston et al., 2003) and the Gao-Zhang (GZ) (Gao and Zhang, 2012) model. The Johnson–Cook (JC) model introduced in 1983 is a widely used model due to its ease of implementation and relative accuracy (Johnson and Cook, 1983, 1985). This is a semi-empirical model which can be calibrated and implemented in numerical analyses. Instantaneous flow stress is expressed as a function of plastic strain, strain rate and temperature, where the effects of work hardening, strain rate hardening and thermal softening are represented in three separate terms. The JC model is commonly utilized in analysis of HSR events such as machining, turning (Jaspers and Dautzenberg, 2002; Umbrello et al., 2007; Maurel-Pantel et al., 2012) and vehicular crash simulations (Mahadevan et al., 2000).

The linear version of JC model is not suitable for analysis of ultra high strain rate (UHSR) deformations such as cold spray impacts. Various modifications to the JC model have been proposed to represent the strain rates that are greater than $10^4 \ s^{-1}$. Tuazon et al. modified the strain rate sensitivity term of the JC model with a logarithmic power-law by adding two material constants (Tuazon et al., 2014), but in the low strain rate regime, the model presents fictitious stress. Chakrabarty et al. developed a modified version taking into account the viscous drag effect by adding an extra term in the strain rate term and incorporated strain gradient plasticity to address the vastly different deformation patterns inside the particle (Chakrabarty and Song, 2020). Other forms of modified JC model includes but are not limited to quadratic equation interpolation of static and dynamic experimental results (Huh and Kang, 2002), incorporation of thermally activated and viscous regimes (Couque et al., 2006) and incorporation of modified-Eyring model (Othman, 2015; Al-Juaid and Othman, 2016; El-Qoubaa and Othman, 2015). These modifications either present inaccurate results or involve too many additional material parameters that require calibration. An effective approach to express the strain rate hardening in the UHSR regime is to use a piecewise linear (bilinear) form in the strain rate hardening term of the JC model (Lesuer et al., 2001; Manes et al., 2013, 2011; Lemiale et al., 2014). This approach is relatively easy to implement without increasing the number of parameters and enables accurate impact simulations (Alizadeh, 2016; Chen et al., 2018; Chen, 2020).

Adiabatic shear instability is commonly observed in high strain rate, extreme plastic deformations (Yan et al., 2021). If the rate of dissipation of the heat generated due to plastic deformation in such deformations is negligible, a localized band of material deforms in adiabatic manner, where thermal softening dominates over hardening mechanisms, hence, triggers an instability. ASI

usually happens in a two-dimensional manner which resembles a band, therefore, it is often referred to as adiabatic shear banding (ASB). ASI is generally undesirable, in forming processes and shielding for ballistic impacts, but could be desirable in some scenarios such as chip forming (Ye et al., 2017, 2018; Ye and Xue, 2019) during which it leads to damage accumulation and shear failure. This unique phenomenon is also implemented in military applications where ASI helps maintain a sharp tip for "self-sharpening" projectiles (Liu et al., 2020; Cheng et al., 2006, 2007). The micro-structure characteristics and evolution of materials under ASI have been studied extensively. Due to the minimal work hardening they experience, metallic glasses are particularly susceptible to ASI; the micro-structure characteristics correlated to ASI in metallic glasses are reported extensively by Jiang et al. (2018, 2019), Xue et al. (2019, 2021), Lu et al. (2018, 2021), Huang et al. (2017), Sun et al. (2019) and others (Khosravani et al., 2021; Zhao et al., 2017; Im et al., 2018, 2020, 2021). Similarly, for nanocrystalline materials (Feng et al., 2017), the presence of ASI has been of great interest in recent years. Advanced characterization methods such as digital image correlation (DIC) have been employed to characterize in-situ shear bands in various materials (Özdür et al., 2021; Özdür and Aydıner, 2022; Shafaghi et al., 2020; Üçel et al., 2019; Kapan et al., 2017; Meredith, 2021). The roles of dislocation slip (Rousselier et al., 2017; Rousselier, 2021, 2022) and twinning, and the balancing act between them in shear localization have been analyzed in depth (Habib et al., 2019; Chen et al., 2019; Edwards et al., 2019a, 2021, 2019b, 2017; Rousselier, 2022, 2021; Rousselier et al., 2017). Whether dynamic re-crystallization is a precursor to or result of localized shear bands is subject to contention. Also, factors influencing the width and spacing of shear bands are of great interest. As an extreme plastic deformation phenomenon, ASB is usually accompanied by high strain rates. Experimental techniques such as compression/torsional Split-Hopkinson-Bar (Bhagavathula et al., 2018, 2022; Zuanetti et al., 2022), Taylor bar tests are often utilized to study the physics involved in this material behavior.

Various criteria for ASI has been proposed in the past decades, where adiabatic deformation process is assumed such as those reported by Culver (1973), and Recht (1964). More involved criteria (Yan et al., 2021) usually take into consideration the thermal/heat transfer aspect of the process, including those proposed by Bai (1982), Roessig and Mason (1999), Clifton et al. (1984) and Molinari (Molinari, 1985). The effect of initial defects such as material porosity is of great concern during high strain rate loading, and in turn often influence the initiation of shear localization (Vishnu et al., 2022a; Marvi-Mashhadi et al., 2021; dos Santos et al., 2021; N'souglo et al., 2021; Vishnu et al., 2022b; Jacques and Rodríguez-Martínez, 2021; Vaz-Romero et al., 2017; N'souglo et al., 2018; Rodríguez-Martínez et al., 2017). For theoretical analysis of ASI/ASB, an accurate depiction of work hardening, strain rate hardening and thermal softening is of importance. Finite element methods are often employed to this end (Horn et al., 2018), both explicit and implicit methods have been utilized so far (Arriaga and Waisman, 2017; Pascon and Waisman, 2021b; You et al., 2021; Berger-Vergiat and Waisman, 2017; Svolos et al., 2020; Pascon and Waisman, 2021a; Svolos et al., 2021; Berger-Vergiat et al., 2019). Material response of metals such as Titanium, Aluminum alloys and steels at high strain rate have been investigated extensively by Fan et al. (2017), Zeng et al. (2020), Meng et al. (2018), Li et al. (2017), Zeng et al. (2021), Xiao et al. (2021) and Habib et al. (2019, 2017, 2021). Both experimental and theoretical analyses were utilized and reported by Ku et al. (2020), Ku (2020).

Constitutive modeling of Aluminum is of great interest, and various models have been proposed and tested to address Aluminum alloys' elastic/plastic (Ku et al., 2020; Kabirian et al., 2014; Iftikhar et al., 2021; Li et al., 2019; Cao et al., 2020; Liu et al., 2022; Li et al., 2021) and damage behavior (Gao et al., 2020; Ying et al., 2019, 2021; Rong et al., 2019; Hu et al., 2017). Among all models, Johnson–Cook (JC) model has been the most commonly used one due to its simplicity and ease of implementation in numerical analysis and interpretation of hardening and softening factors. Various modifications to JC model have been proposed further addressing in-depth material behaviors such as strain rate sensitivity in a broad temperature range (Li et al., 2017). Although, it has been a preconceived notion that ASI is the driving mechanism behind bonding during cold spray deposition, the very presence and nature of it is still up to debate (Yan et al., 2021; Hassani-Gangaraj et al., 2018). This paper aims to investigate the presence of ASI during Al-6061 powder particle impacts.

To this end, an investigation into the material behavior during the high velocity impact of a single micron-scale, Al-6061 particle is presented. Impacts on a hard sapphire and an Al-6061 surfaces are considered. In previous work, the authors have shown that in Al-on-sapphire impacts, a small volume of the material loses its strength due to high temperatures associated with plastic work. This behavior was deemed to be material instability (Chen et al., 2018). Here a mathematically and physically accurate material instability criterion from Roessig and Mason (1999) is used to assess material behavior for impacts on both types of surfaces. Results from Chen et al. (2018) are reassessed and new experiments and simulations are conducted for Al-on-Al impacts.

2. Materials and methods

2.1. Laser induced single particle impact experiments

Laser-induced projectile impact test (LIPIT) was used to study impact of micron scale Al-6061 particles on an Al-6061 substrate. Similar experiments for the impact of Al-6061 particles on a sapphire was reported in Xie et al. (2017). In this set-up single Al-6061 particles are accelerated by a rapidly expanding PDMS film (Fig. 1a) to velocities in the range of 50–1200 m/s (Lee et al., 2012, 2014; Chen et al., 2018). The flight history of the particles are captured by ultrafast stroboscopic imaging with ~100 fs light pulses ($\lambda = 740$ nm) (Chen et al., 2018). Impact and rebound velocities of the impinging particles are deduced from the captured frames as shown in Fig. 1(b).

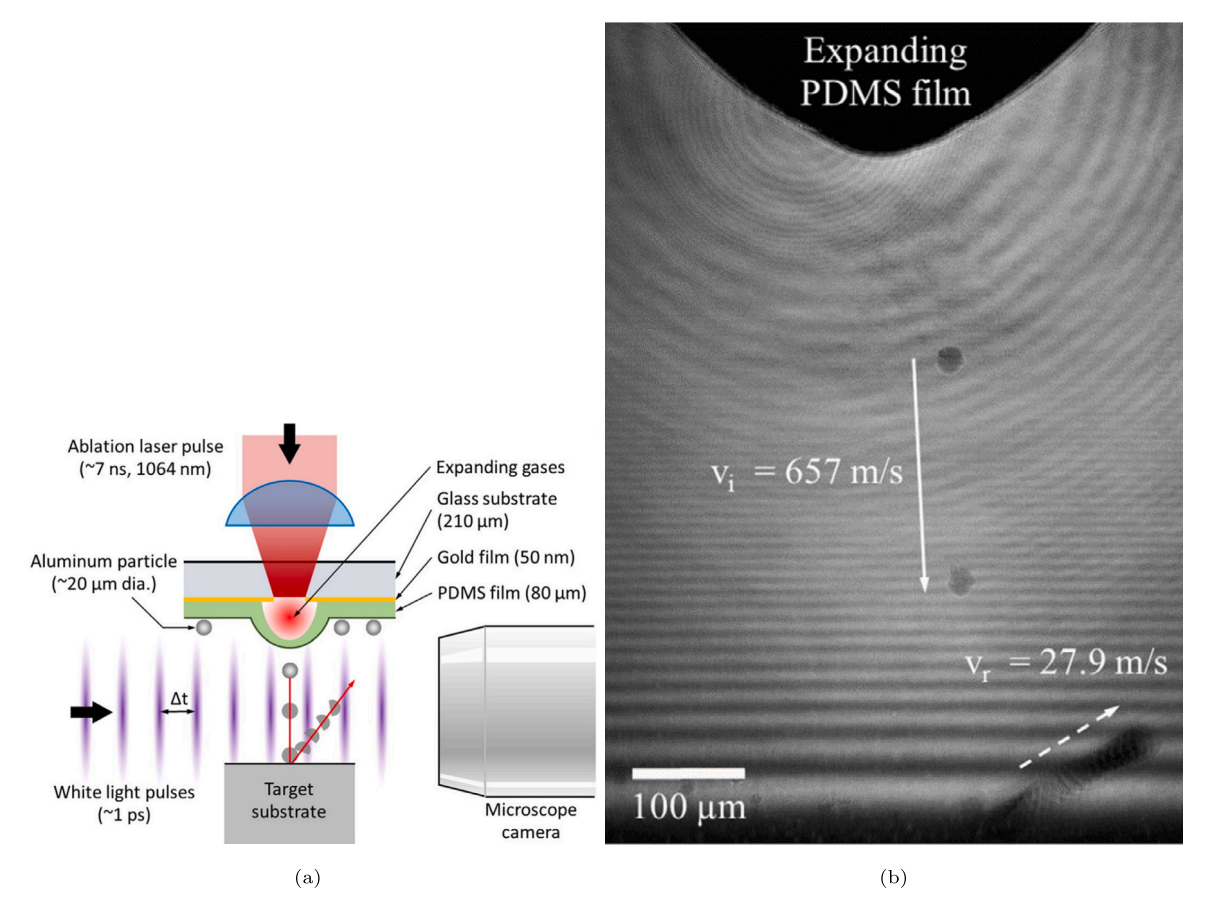


Fig. 1. (a) The α -LIPIT setup used in the experiments. Xie et al. (2017) (b) The collision and rebound of an Al-6061 particle with the sapphire substrate captured by multiple exposure photography (Chen et al., 2018). Fig. 1 is printed with permission.

2.2. Finite element simulations

Mechanics of particle impact was simulated by using the commercially available finite element software Abaqus-Explicit 2022 (Anonymous, 2022). In the elastic regime, the material was modeled as linear elastic and isotropic. In the plastic regime, isotropic hardening with strain, strain-rate and temperature dependent flow stress was used. Material damage was simulated by using a shear damage model. The particle–substrate interface included, contact, friction and cohesion effects. Stability of the material points (nodes) during deformation was monitored at each iteration step. Details of these material models are described in the next sections.

Yildirim et al. (2011a) showed that the choice of modeling approach should be considered carefully for high velocity impact simulations in order for the predicted shapes of the deformed particles to remain similar to the experimental observations. In particular, they showed that an axisymmetric, Lagrangian model of the deformation process results in excessive deformation of the elements; the predictions of the deformed shapes are not even remotely similar to experimentally observed ones; and excessively deformed elements have near zero Jacobians which render the results unreliable. Following their recommendation, a 3D quarter symmetric (Fig. 2), Lagrangian model with element removal capability was used in this work. The effects of element removal are discussed in Appendix and Yildirim et al. (2011a), whereas successful implementation of this technique for high velocity impacts are demonstrated in Chen et al. (2018), Alizadeh (2016), Chen (2020).

Fixed boundary conditions were assigned to the peripheral and bottom boundaries of the substrate, whereas the two lateral surfaces were assigned symmetry boundary conditions. The effects of air-drag and body forces were neglected. Particle diameter is assumed to be 19 μ m for all cases. A dense mesh was assigned near the impact site, while the outer region of the substrate was discretized with larger elements. A geometrical tie constraint was assigned between the dense and sparse mesh zones to ensure conforming deflection. The element size in the particle and dense mesh zone in the substrate was set to be 1/25 of the particle diameter D_p , while the element size of the sparse mesh zone was approximately 10 times larger. The size of the substrate was chosen such that the reflected waves do not reach the impact site within the first 100 ns following impact. Thus the impact events were simulated to ensure rebounding waves from the model boundaries would not interfere with the impact mechanics (Yildirim et al., 2015; Alizadeh, 2016; Yildirim, 2013). A first order, 8-node continuum element C3D8RT (Anonymous, 2022) which uses reduced

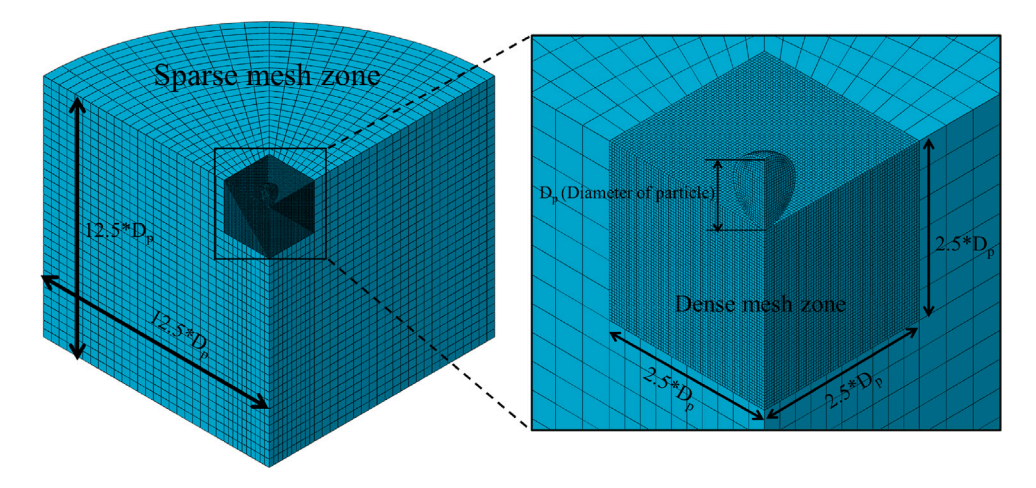


Fig. 2. Geometry of the quarter-symmetric model for single particle impact FEM simulation.

integration and capable of coupling thermal and solid state physics was adopted across the entire model. For the interaction between the particle and the substrate, Abaqus' built-in general contact was employed with a friction coefficient of 0.7. Coulomb friction model was adopted for tangential behavior assuming the same coefficient of friction in all directions. During plastic deformation, around 10% of plastic energy is spent on defect generation and the rest is dissipated in the form of heat generation (Meyers, 1994). Therefore, the Taylor–Quinney coefficient (β), which represents the ratio of plastic work converted to heat is assumed to be 0.9. Both the particle and substrate were assumed to be at room temperature (293 K) initially which corresponds to the ambient temperature of the experimental environment.

2.3. Material models and properties

Temperature dependent material properties of Al-6061, given in Table 1, were imported from the MPDB material database (Anon, 1998) and previous literature (Manes et al., 2011, 2013; Munro, 1997). An in-depth analysis of the effects of material temperature dependency of Al-6061 was reported by Chen (2020). The bilinear-JC flow stress model was used in the following form (Chen et al., 2018; Alizadeh, 2016),

$$\sigma_Y = \left(A + B\varepsilon_p^n\right) \left(1 + C \ln \frac{\dot{\varepsilon}_p}{\dot{\varepsilon}_0}\right) \left(1 - \left(\frac{T - T_R}{T_m - T_P}\right)^m\right),\tag{1}$$

and

$$C = \begin{cases} C_1 \text{ and } \dot{\varepsilon}_0 = 1 & \text{if } \dot{\varepsilon}_p < \dot{\varepsilon}_c \\ C_2 \text{ and } \dot{\varepsilon}_0 = \dot{\varepsilon}_c & \text{if } \dot{\varepsilon}_p > \dot{\varepsilon}_c \end{cases}$$
 (2)

 σ_Y is the flow stress, A, B, C_1 , C_2 , n, m, and $\dot{\epsilon}_c$ are the empirically determined material parameters, ϵ_p is the equivalent plastic strain, $\dot{\epsilon}_p$ is the equivalent strain rate, $\dot{\epsilon}_0$ is the reference strain rate, T_m is the melting temperature of the material and T_R is the reference temperature. The effects of strain hardening, strain rate hardening and thermal softening are multiplied in this model. Parameters of bilinear-JC model were calibrated for Al-6061 and reported by Xie et al. (2017) and Chen et al. (2018), Alizadeh (2016). For the linear-JC model the constant $C_2=0$ and the variable $\dot{\epsilon}_p$ is irrelevant. The material properties for the two models are reported in Table 1.

2.4. Material damage model

Yildirim et al. showed that material failure can be expected in the excessively strained regions during particle impact events (Yildirim et al., 2011a). If an excessively distorted element is kept in the model, it will have erroneous load carrying capacity; the minimum dimension (thickness, width or length) of the element will go to near zero values, resulting in a zero or negative Jacobian. Extremely small element dimensions will reduce the stable time increment of the explicit solver to an infinitesimal level triggering a numerical error that terminates the analysis. Removing elements that lose their load carrying capability from the assembly helps to avoid singularities caused by excessively distorted elements (Keeler and Backofen, 1963; Marciniak and Kuczyński, 1967). Therefore, in this study, a simplified version of shear-damage model was adopted to simulate material damage as a means to mitigate the effects of excessive element distortion in the Lagrangian modeling approach. The criterion for initiation of damage is described as follows:

$$\omega = \sum \left(\Delta \varepsilon_p / \varepsilon_f \right) = 1 \tag{3}$$

Table 1

Material properties of the particle and the substrate (Al-6061) at room temperature (293 K). Subscript, denotes the property's room temperature value. The temperature dependence of these material properties is determined as described by Yildirim et al. (2011a). Parameters calibrated for the bilinear version of JC model are reported by Xie et al. (2017), Alizadeh (2016), Chen et al. (2018) Parameters for the linear version of the JC model are reported by Lesuer et al. (2001). Material properties for sapphire substrate are reported by Chen et al. (2018).

Particle and substrate (Al-6061) (Chen et al., 2	* * *	
E_r , Elastic modulus, GPa	69.11	
ρ_r , Mass density, kg/m ³	2700	
v_r , Poisson's ratio	0.331	
α_r , Coefficient of thermal expansion, K^{-1}	2.23×10^{-5}	
k_r , Thermal conductivity, W/m K	154	
c_r , Specific heat, J/kg K	1009	
β , Inelastic heat fraction (constant)	0.9	
Substrate (Sapphire) (Chen et al., 2018)		
E, Elastic modulus, GPa	345	
ρ, Mass density, kg/m ³	3980	
v, Poisson's ratio	0.29	
α , Coefficient of thermal expansion, K^{-1}	6.98×10^{-6}	
k, Thermal conductivity, W/m K	23	
c, Specific heat, J/kg K	896	
JC-model parameters for Al-6061		
	Bilinear (Alizadeh, 2016; Xie et al., 2017; Chen et al., 2018)	Linear (Lesuer et al., 2001)
A (MPa)	270	324
B (MPa)	154.3	114
C_1	2×10^{-3}	2×10^{-3}
C_2	2.9×10^{-2}	N/A
m	1.42	1.34
n	0.239	0.42
$\dot{arepsilon}_0$	1	1
$\dot{arepsilon}_c$	597.2	N/A
T_R (K)	293	293

where $\Delta \epsilon_p$ is the increment of the equivalent plastic strain, ϵ_f is the failure shear strain, which can be a function of equivalent plastic strain and stress triaxiality. Numerical experiments show that using a constant value of $\epsilon_f=3$ successfully predicts the deformed Al-6061 particle shapes (Alizadeh, 2016; Chen et al., 2018; Chen, 2020). The damage parameter ω cumulatively increases as plastic deformation progresses during impact, and after damage initiates the load carrying capacity of the material progressively degrades. This process is modeled with a displacement or energy law (Li, 2001). However, in this study, the energy dissipation before full material failure was assumed zero. Thus the material is completely damaged immediately following the onset of damage, leading to removal of the corresponding element from the simulation. Material follows plastic flow rule up until an equivalent plastic strain of 3 and immediately loses its load carrying capacity completely, thereafter.

2.5. Cohesive zone modeling and calibration of cohesion parameter

The cohesive zone model (CZM) proposed by Needleman (Needleman, 1990) was used to model the bonding and detachment of particle–substrate and/or particle–particle interfaces (Lin et al., 2019; Chen et al., 2018; Yildirim et al., 2011b, 2015; Yıldırım et al., 2012). In CZM a traction–separation law governs the relationship between the cohesive traction, σ , and interface separation, δ as shown in Fig. 3. The area under the traction–separation curve represents the cohesion energy (critical strain energy release rate) G_c of the interface. The interface behaves elastically when the interface separation is less than the critical separation ($\delta < \delta_c$). The cohesive traction that corresponds to the critical separation is σ_c . When the interface separation is greater than critical ($\delta > \delta_c$), the cohesive strength starts to degrade. The cohesive behavior is terminated once the failure separation δ_f is reached where the cohesive traction becomes zero. If the loading is reduced in the range $\delta_c < \delta < \delta_f$ the unloading will follow a new route as demonstrated by the red line in Fig. 3, but a portion of the cohesion energy G_c will have been lost. In finite element simulations, this model is implemented on the individual pairs of nodes. In impact simulations, breaking of the interfacial cohesion depends on the local energy balance at each material point (Yildirim et al., 2011b, 2015; Yıldırım et al., 2012). If the local elastic rebound energy is greater than the local cohesion energy G_c then the material point can debond. If the entire interface experiences debonding then the particle will rebound from the surface. Built-in surface based cohesive behavior of Abaqus is used adopted to simulate the cohesion between particle and the substrate. All element surfaces in the particle and in the dense mesh zone of the substrate are activated for the cohesive behavior in contact.

2.6. Material instability

Plastic deformation of metals is present in many highly dynamic scenarios, especially manufacturing processes and ballistic impacts. Adiabatic shear band/localization may occur during plastic deformation due to high loading rates, geometry constraints

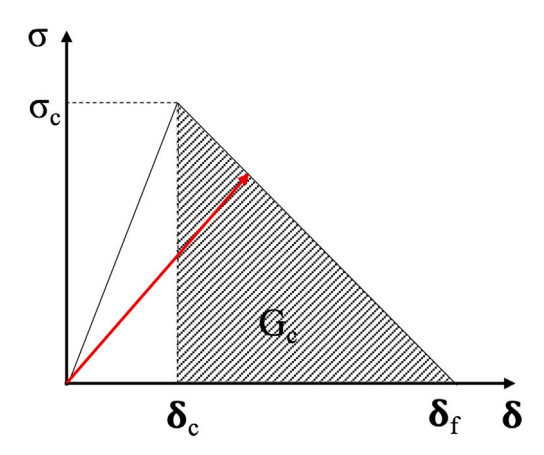


Fig. 3. Traction-separation law adopted in cohesive zone modeling.

or both. Severe shear deformation is present within the adiabatic shear bands where local plastic heat accumulates drastically, hence thermally softening the material, which in turn leads to a self-driven deformation mechanism (Roessig and Mason, 1999). The process is adiabatic since the time frame of the phenomenon is very short and heat does not have sufficient time to be conducted away. The width of adiabatic shear band is usually in the range of 10 to 100 µm (YL et al., 1992). Material undergoing ASI would collapse along the shear localization band. During such an event, the thermal softening is so drastic that it overcomes accompanying strain hardening and strain rate hardening (Wright and Batra, 1985).

In numerical simulations, Zener and Hollomon (1944) proposed a quantitative criteria for ASI, which states that a material point becomes unstable during loading, if the rate of change of the flow stress with respect to plastic strain is negative, i.e. $\frac{\partial \sigma_{\gamma}}{\partial \varepsilon_{p}} < 0$, while the strain rate, ε_{p} , and the rate of change of strain rate, ε_{p} , are non-negative. Considering the flow stress depends on the plastic strain, strain rate and temperature, Roessig et al. presented a quantitative criteria for the occurrence of ASI as follows (Roessig and Mason, 1999):

$$\left(\frac{\partial \sigma_{Y}}{\partial \varepsilon_{p}}\right)_{\tilde{\chi}} = \left(\frac{\partial \sigma_{Y}}{\partial \varepsilon_{p}}\right)_{\varepsilon} + \left(\frac{\partial \sigma_{Y}}{\partial \varepsilon_{p}}\right)_{\varepsilon} \frac{d\dot{\varepsilon_{p}}/dt}{d\varepsilon_{p}/dt} + \left(\frac{\partial \sigma_{Y}}{\partial T}\right)_{\varepsilon_{p},\varepsilon_{p}} \frac{\beta \sigma_{Y}}{\rho c_{p}} \le 0 \tag{4}$$

$$\dot{\varepsilon_p} \ge 0 \quad \& \quad \dot{\varepsilon_p} \ge 0$$
(5)

where \tilde{x} is the specific location of the material point, σ_Y is flow stress, ε_p is shear strain, T is temperature, ρ is mass density, c_p is specific heat and β is the fraction of plastic work that turns into heat energy. The two constraints rule out the situation where the criterion may be satisfied when the material is undergoing unloading.

Presence of ASI in high velocity impact of micron scale metal particles with metal substrates has been predicted in finite element simulations by several authors (Assadi et al., 2003; Chen et al., 2018; Champagne et al., 2005; Grujicic et al., 2004). In these works, the temperature history of certain, critical material points has been monitored. These impact simulations show a sudden rise in temperature during impact. As the only source of heating in these simulations is due to plastic action in the material, this temperature rise has been reported as the indication of ASI. In what follows we use the ASI criteria given in Eqs. (4) and (5) to assess whether continuum level simulations predict ASI in impact of Al-6061 particles on Al-6061 substrates (Al-on-Al) and Al-6061 particles on sapphire substrates (Al-on-sapphire).

3. Results and discussion

3.1. Rebound and cohesion of particles

The global energy dissipation in high velocity impact experiments are assessed by using the coefficient of restitution (e) of the particles. Experimentally, e is defined as the ratio of the rebound velocity V_r to the impact velocity $e = V_r/V_i$ determined by image analysis of the α -LIPIT experiments. Numerically, the rebound velocity is calculated by averaging the component of the velocity vector normal to the substrate at three different points (north pole, south pole and center) of the particle.

Fig. 4(a) shows e as a function of impact velocity, $e = e(V_i)$, for Al-on-sapphire impacts. These results have been reported by Xie et al. (2017) and repeated here for comparison. In this case we see that e decreases monotonically until 500 m/s and remains small and non-zero until the highest tested velocity value of 950 m/s. This behavior is attributed to increasing levels of plastic dissipation in the particle (Yildirim et al., 2017). No bonding between the sapphire substrate and the Aluminum particles was observed. Simulations ($G_c = 0$) show very reasonable prediction of e as function of impact velocity.

The e values for Al-on-Al impacts are shown in Fig. 4(b). In this case we observe that e decreases monotonically until impact velocity of 400 m/s. Thereafter, e is reduced at a slower rate, due to increased plastic dissipation, until it abruptly becomes zero near the impact velocities of 810–820 m/s, indicating that the particle bonds to the substrate.

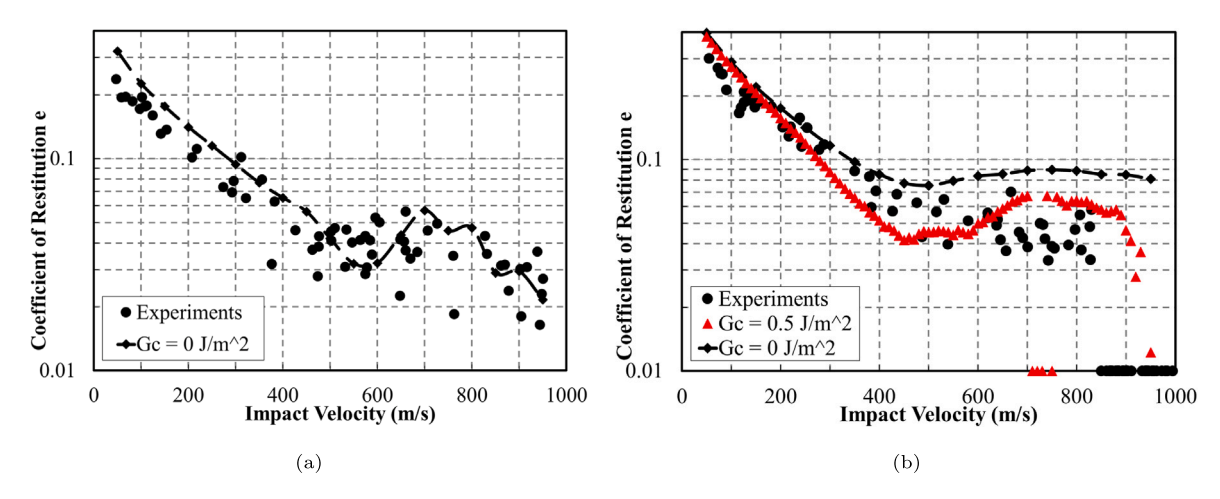


Fig. 4. Comparison of the experimentally measured and simulated coefficient of restitution as a function of impact velocity for (a) Al-on-sapphire (Chen et al., 2018) and (b) Al-on-Al impact. In part (a) the cohesion energy was not considered. In part (b) the effects of using zero cohesion energy and $G_c = 0.5 \text{ J/m}^2$ are presented. Fig. 4(a) is printed with permission.

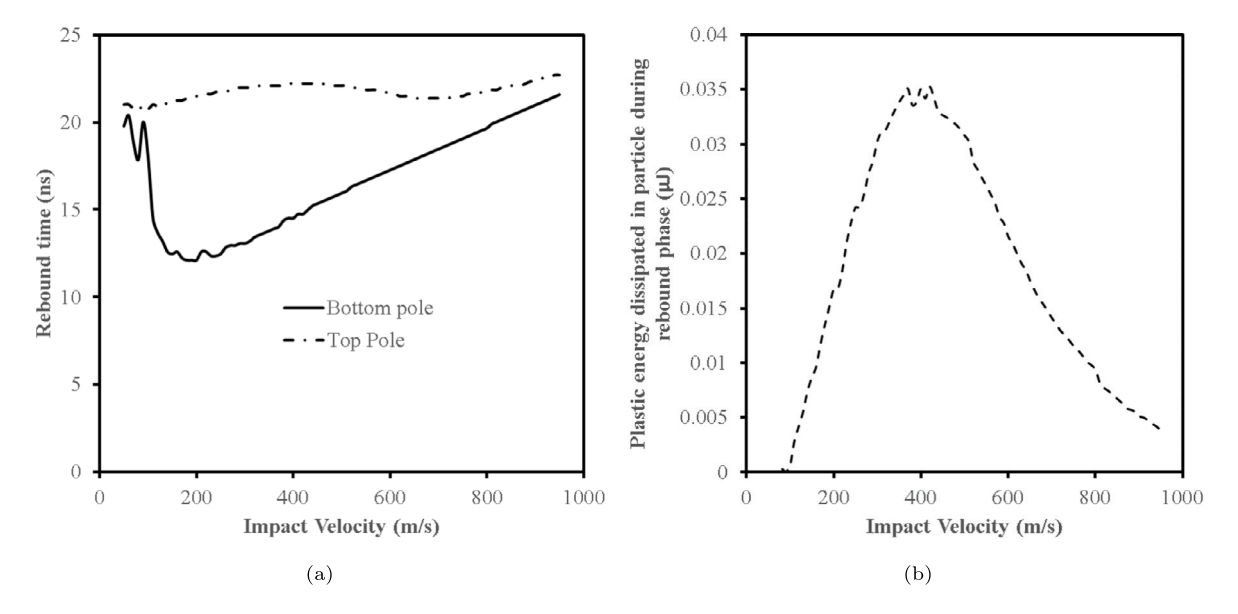


Fig. 5. Al-on-Al impacts: (a) The rebound instance of the north (top) and south (bottom) poles of the particle for different impact velocities. (b) The level of plastic energy dissipated in the particle during the rebound phase for different impact velocities.

In order to simulate the observed cohesion behavior, eight different cohesion energy values, ranging from 0 to 6 J/m² were tested, while keeping the cohesive strength constant at $\sigma_c = 300$ MPa which is chosen according to tensile strength of Al-6061. Among the computed e behavior at different cohesion energy levels, $G_c = 0.5$ J/m² demonstrates the best match to experimental results. A more in-depth investigation of the cohesion parameters was reported by Chen (Chen, 2020).

The coefficient of restitution as a function of impact velocity (V_i) is an indication of the degree of plastic deformation in the system. The $e(V_i)$ relationship can be separated into the following four regimes based on the material response: elastic deformation (ED), elastic–plastic deformation (EPD), finite-plastic deformation (FPD) and deeply-plastic deformation (DPD) (Yildirim et al., 2017). The particle behaves purely elastically in the ED regime. In the EPD and FPD regimes, increasingly larger fraction of the particle volume experiences plastic deformation during impact, and in the DPD regime the entire particle is plastically deformed. By using the parameters given in Table 1 it can be shown that the ED-to-EPD transition occurs at the impact velocity of 0.078 m/s. The FPD-to-DPD transition depends on the magnitude of the dynamic yield stress. For example, this transition occurs at the impact velocity of 241 m/s for yield stress value of 270 MPa and 341 m/s for 540 MPa (Yildirim et al., 2017).

Yildirim et al. attributed the non-monotonic dependence of e on V_i as shown in Fig. 4 to the changes in plastic dissipation characteristics of the particle (Yildirim et al., 2017). The *rebound instant* of a material point is defined as the moment when the velocity of that point is reversed. The rebound instants of the north and south poles of the particle are plotted in Fig. 5(a). This

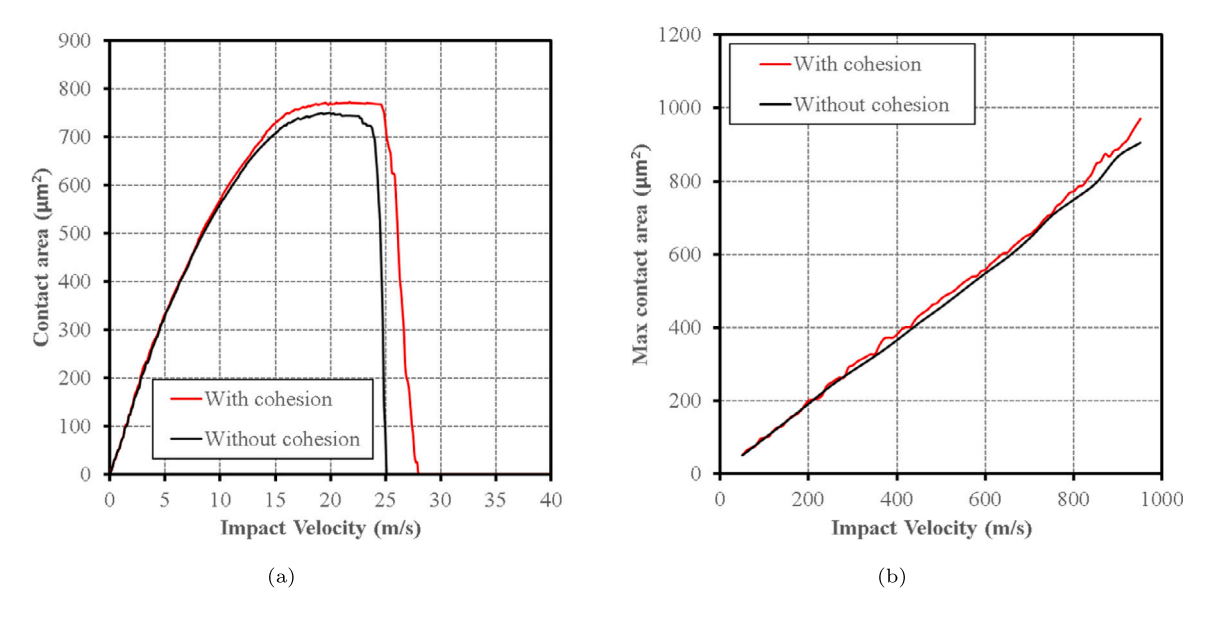


Fig. 6. Al-on-Al impacts: Contact area and cohesion energy evolution during Al-6061 on Al-6061 impacts (a) Effect of cohesion energy $(G_c = 0.5 \text{ J/m}^2)$ on the evolution of contact area with 800 m/s impact. (b) Maximum contact area with and without cohesion as a function of impact velocity. Note that contact area is a secondary variable in finite element analysis, and therefore it involves a larger uncertainty. The non-smooth variations in contact area with cohesion is attributed to the numerical error related to contact area calculations. Nevertheless, the contact area with cohesion is generally larger.

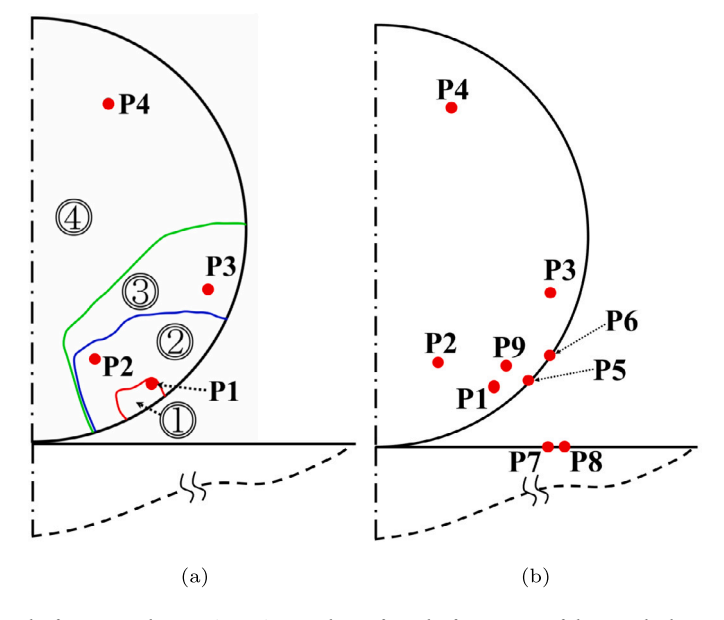


Fig. 7. (a) Al-on-sapphire impacts: The four material points (P1-P4) were chosen from the four regions of the particle that experience different levels of damage and flow stress behavior (Chen et al., 2018). (b) Al-on-Al impacts: Locations of the representative material points inside the particle and substrate. P5 and P6 are the two points where the most extreme material behavior is observed inside the particle, and P7 and P8 are the two points where the most extreme material behavior is observed inside the substrate. P9 is the characteristic point analyzed in Al-on-Al impact simulation with classic JC model. Fig. 7(a) is printed with permission.

shows that in the velocity range of $\sim 100-\sim 700$ m/s, the south pole of the particle starts to rebound while the north pole is still moving towards the substrate. The gap between the rebound instants closes with increasing impact velocity, indicating the particle's top and bottom poles start to rebound at the same instant and move with the same speed afterwards. The *plastic energy dissipation* in the particle during the rebound phase is computed and plotted as a function of impact velocity in Fig. 5(b). This energy reaches a peak near the velocity of 400 m/s, which is very close to where coefficient of restitution begins to plateau in Fig. 4. Near this velocity the particle starts to dissipate less plastic energy during rebound phase as its deformation becomes increasingly severe. This velocity point is also close to the beginning of the DPD regime.

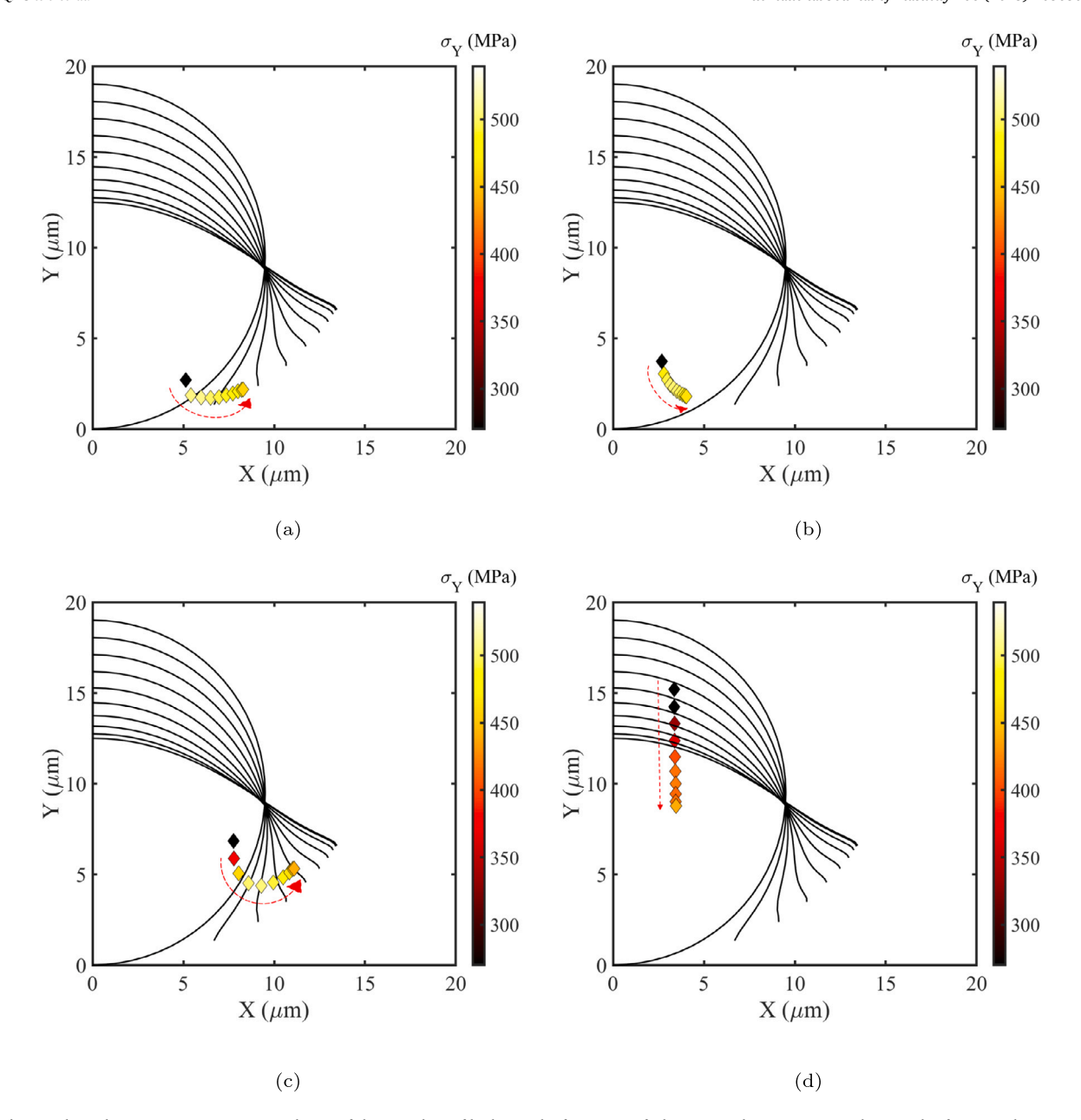


Fig. 8. Al-on-Al impacts, points P1-P4: Evolution of the particle profile during the first 24 ns of Al-6061 on Al-6061 impact with intervals of 2.4 ns. The impact is along the negative Y direction with a velocity of 800 m/s. The particle profiles are aligned at their respective south poles for ease of reading. The particle profiles seem to intersect at a common point, but close inspection reveals that they do not. This coincidence is irrelevant to the kinematics of the particle. The bottom edges of the particles are hidden in these figures to avoid crowding. The markers represent the location of each material point relative to the corresponding profile over the impact duration. The markers are color-coded to reflect the instantaneous yield stress and the direction of the material points' trajectories are marked with arrow in each figure. (a) P1, (b) P2, (c) P3, (d) P4.

Fig. 4(b) shows a difference in the predicted coefficient of restitution for cases with and without cohesion. This difference is small for small velocities and grows after $V_i = 200$ m/s. This difference is attributed to the extra work that the system has to perform when the cohesion is included in the simulations. Fig. 6(a) shows the results of cohesion on the contact area during impact. The contact area grows as the impingement of the particle progresses and reaches its maximum at around 17 ns, followed by a quick rebound around 25 ns. The case with cohesion has a slightly larger contact area and the interactions of the two bodies last slightly longer. Therefore, when cohesion is introduced into the solution more energy is spent to form larger contacts, and more energy is dissipated. This ultimately results in lower rebound velocity or e as reported in Fig. 4(b). The maximum contact area is plotted for different impact velocities in Fig. 6(b). The maximum contact area increases almost linearly as a function of impact velocity with or without cohesion, but the contact area with cohesion is slightly larger, as expected.

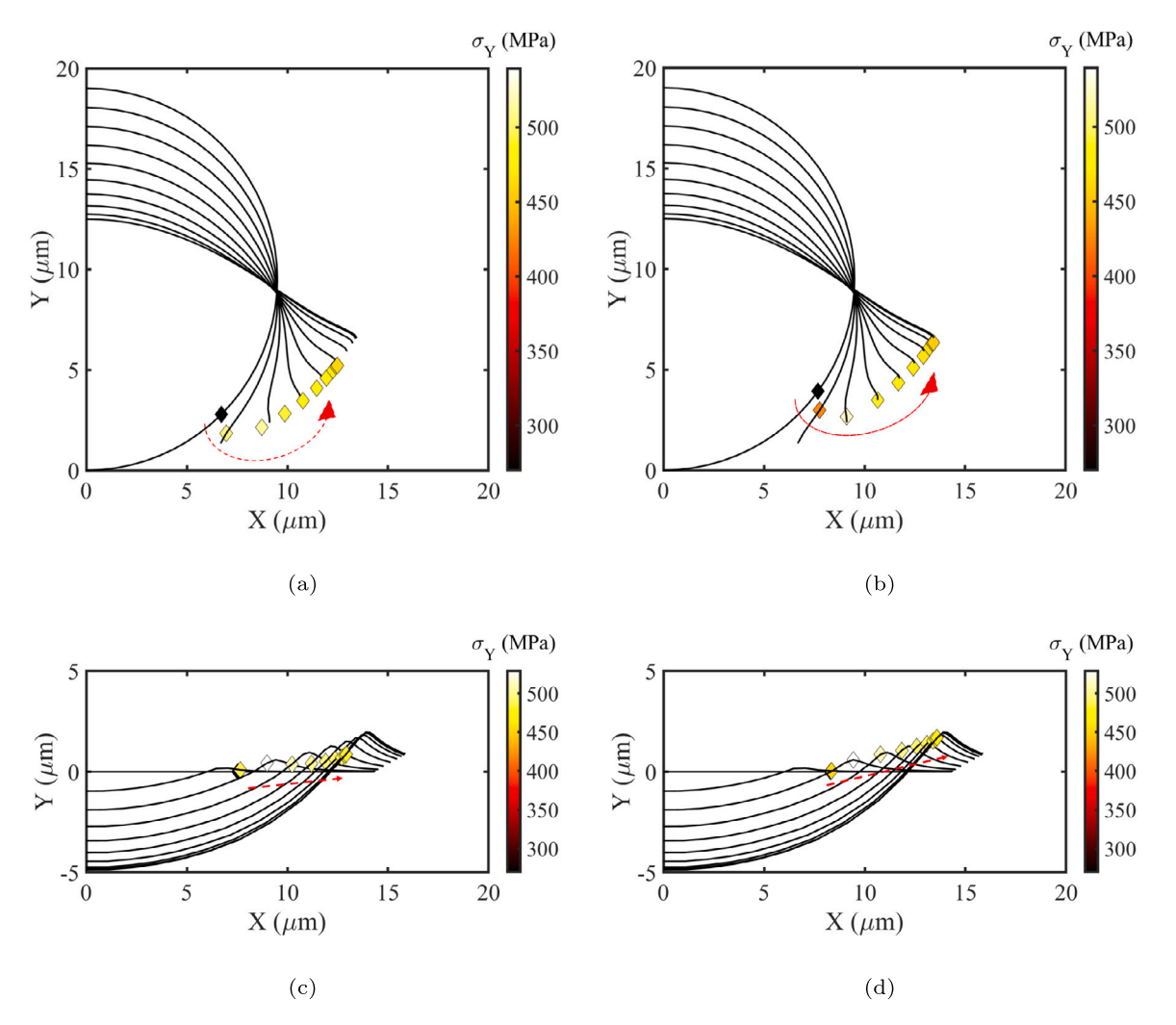


Fig. 9. Al-on-Al impacts, points P5–P8: Evolution of the particle and substrate crater profiles during the first 24 ns of Al-6061 on Al-6061 impact with intervals of 2.4 ns. The impact is along the negative Y direction with a velocity of 800 m/s. The particle profiles as shown in (a) & (b) are aligned at the bottom pole of the particle, while substrate crater profiles are not aligned and reflect their actual location as shown in (c) & (d). The markers represent the location of each material point relative to the corresponding profile over the impact duration. The markers are color-coded to reflect the instantaneous yield stress and the direction of the material points' trajectories are marked with arrow in each figure. (a) P5, (b) P6, (c) P7, (d) P8.

Chen et al. (2018) investigated the potential for ASI in Al-on-sapphire impact experiments reported by Xie et al. (2017). They used finite element simulations to monitor history of the flow stress, temperature, strain and strain rate of all material points (element nodes) in the particles during impact (Chen et al., 2018). This analysis showed that there is a relatively small region in a spherical particle where the flow stress vanishes precipitously during impact. Based on these predictions, it was concluded that the material in regions-1 and -2 of the particle shown in Fig. 7(a) experiences adiabatic shear instability.

In this work, displacement histories of the same four representative material points, P1–P4 are also followed for Al-on-Al impacts as shown in Fig. 8,¹ and four additional points, P5–P8, are plotted in Fig. 9. These four points were chosen by monitoring the stress histories of all the material points (nodes) in the particle and the substrate. Points P5 and P6 are the two points where the most extreme material behavior is observed inside the particle, and P7 and P8 are the counterparts for the substrate. It is revealed that all four points P5–P8 end up near the jetting lip as shown in Fig. 9. Figs. 8 and 9 also show the yield stress histories of these points. This shows that the yield stress varies between 270 and 500 MPa during deformation, but no evidence of reduction in flow stress is observed in Fig. 8. Compared to the Al-on-Sapphire impacts presented by Chen et al. (2018), deformation of the same four points is considerably less severe, and unlike the Al-on-sapphire cases, the points P2 and P3 do not move into the contact interface.

Evolution of the equivalent plastic strain ϵ_p and hydrostatic pressure (p) in the first 25 ns after impact are plotted in Figs. 10 and 11 for an impact velocity of 900 m/s. The movement of the lines that define the elements indicate the flow of material during

¹ Close-up of Figs. 8 and 9 show that the particle profiles that appear to intersect at a common point in fact do not and this appearance is only coincidental.

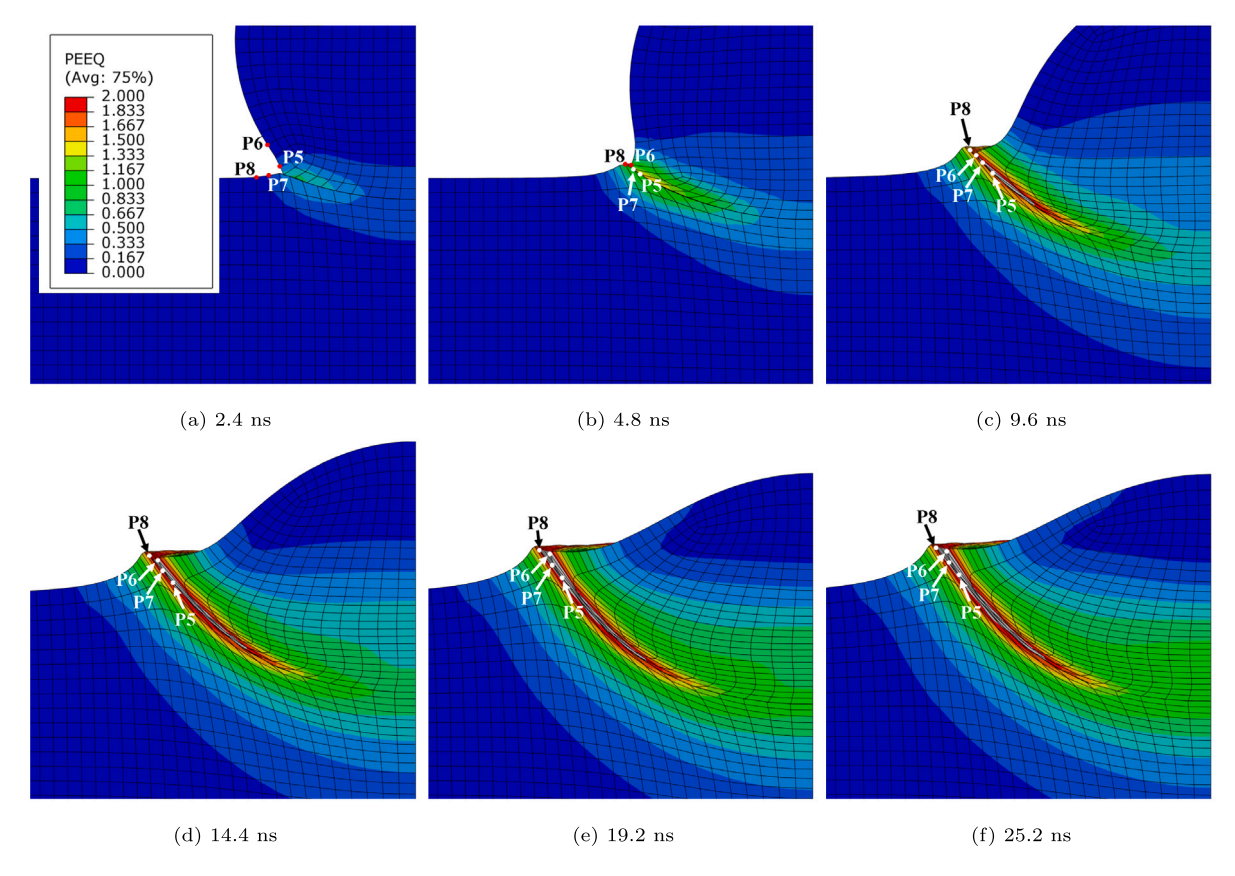


Fig. 10. Evolution of the equivalent plastic strain in the first 25 ns, for Al-on-Al impact at $V_i = 900$ m/s. (a) 2.4 ns, (b) 4.8 ns, (c) 9.6 ns, (d) 14.4 ns, (e) 19.2 ns. (f) 25.2 ns.

this impact: material near the south pole of the particle experiences compression; and, the material in the outer edges of the contact area experiences increasing amounts of shear. The maximum plastic strain is also accumulated in this region. These results draw interesting parallels with the experimental observations of Evans et al. (2019) who observed evidence of metallurgical bonding and dynamic crystallization in the outer periphery of the contact interface where the shear strains appear to be high, and no evidence of bonding in the south pole.

Upon impact a compressive (p > 0) shock wave propagates both into the particle and substrate from the contact interface, and the lower portion of the particle and the top of impact crater are entirely in a compressive state (Fig. 11). At around 10 ns, the pressure around the jetting tip starts to transition from compressive to tensile (p < 0). During the next 12 ns, the hydrostatic pressure in the those regions becomes tensile. A similar phenomenon is observed for Al-on-Sapphire impact considerably earlier, around 7–10 ns (not shown). The jetting observed in the outer periphery of the contact region at these high velocities appears to be the result of the material flow that come from within the particle, but interestingly it is also accompanied with a tensile hydrostatic pressure as highlighted by Hassani-Gangaraj et al. (2018). As it will be shown later in this paper, material instability is not required for it to flow in the interface in the manner shown in Figs. 10 and 11. Material flow within a particle and a substrate was extensively investigated by Yildirim et al. (2017) who made similar observations.

3.2. Comparative evaluation of ASI in Al-on-Al and Al-on-sapphire impacts

To gain further insight into evolution of flow stress in Al-on-Al impacts, the temporal change of equivalent plastic strain ϵ_p , strain rate $\dot{\epsilon}_p$, temperature T and the instantaneous yield stress σ_Y of all the material points in the model are monitored for a broad range $(0 < V_i < 900 \text{ m/s})$ of impact velocities. Since the particle rebounds or bonds with the substrate within 30 ns, only the first 30 ns of the impact are analyzed. The effects of these variables are presented according to their influence on the flow stress as represented in Eq. (1). The time histories of strain hardening $(1 + B/A\epsilon_p^n)$, strain rate hardening $(1 + C \ln \dot{\epsilon}_p/\dot{\epsilon}_0)$ and temperature softening $(1 - \left(\frac{T - T_R}{T_m - T_R}\right)^m)$ terms of the JC-model are computed for all material points.

These variables are plotted in Fig. 12 for points P5–P8 for an impact velocity of 800 m/s. As mentioned above, the points that

These variables are plotted in Fig. 12 for points P5–P8 for an impact velocity of 800 m/s. As mentioned above, the points that show the most thermal softening are P5 and P6 in the particle and P7 and P8 in the substrate. Note that points P1–P4, demonstrate negligible decrease in flow stress due to thermal softening. For Al-on-Al impacts, thermal softening effect is much less prominent

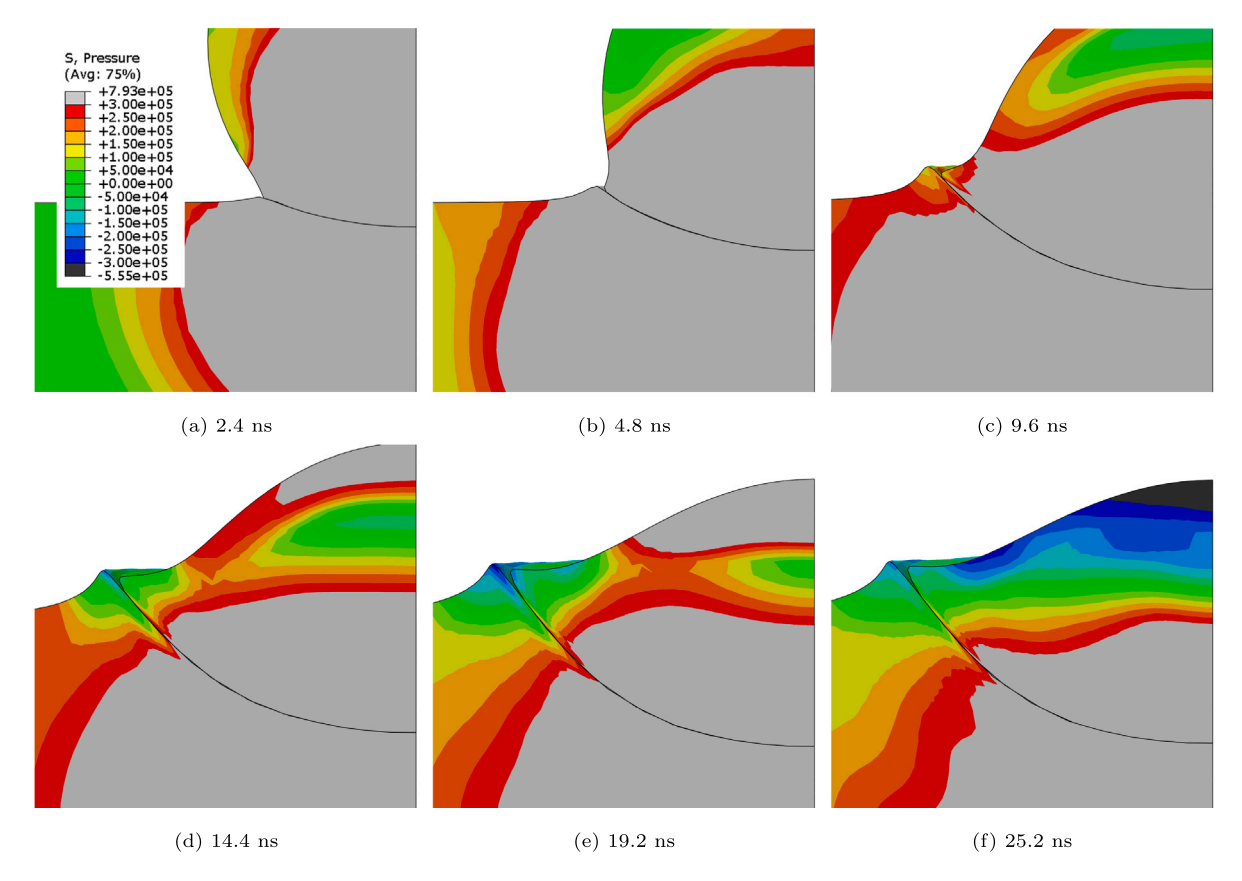


Fig. 11. Al-on-Al impact: Evolution of hydrostatic pressure inside the particle and substrate during the first 26.4 ns in a 900 m/s impact. (a) 2.4 ns, (b) 4.8 ns, (c) 9.6 ns, (d) 14.4 ns, (e) 19.2 ns, (f) 25.2 ns.

when compared to that of Al-on-sapphire impact cases. Details are omitted here due to space constraints, but can be found in Chen (2020).

Fig. 12 also shows that the flow stress increases very rapidly in the first 5–6 ns after impact and gradually drops until the particles rebound. The fluctuations seen in flow stress and the strain rate hardening term after ~ 25 ns are due to the internal wave reflections after the particle rebounds. Noting how the yield stress and strain rate hardening overlap in the first few ns following impact, it can be stated that the rapid rise in the flow stress is initially dominated by strain rate hardening. As the strain rate hardening contribution is reduced, the strain hardening contribution kicks in and thus the yield stress continues to increase for up to 5 ns. Note that strain hardening continues up to 15 ns after initial impact. While these terms show a rapid increase, thermal softening also becomes prominent. Nevertheless, this term settles to a finite trend, and unlike the Al-on-sapphire impacts (Chen et al., 2018), no evidence of significant reduction in yield stress is predicted.

Time histories of the flow stress, strain hardening, strain rate hardening and thermal softening terms in Al-on-Al impacts for point P5 are plotted in Fig. 13 for a wide range of impact velocities. The instantaneous yield stress shown in Fig. 13(a) drops at impact velocities higher than 700 m/s, after the initial increase due to impact loading. The rate of flow stress drop is approximately 20 MPa/ns which is much lower than that from corresponding Al-on-sapphire impact cases (Chen et al., 2018; Xie et al., 2017; Chen, 2020). Figs. 13(b)–13(d) show that this material point experiences work hardening and strain rate strengthening, but at the same time relatively high thermal softening, resulting in the overall drop in the yield stress observed in Fig. 13(a). Point P6 in the particle behaves in a similar way and points P7 and P8 in the substrate demonstrate even lower rate of drop in the flow stress. Time history plots similar to Fig. 13(a) for Points P6–P8 are omitted for space considerations, but can be found in Chen (2020). By analyzing all the nodes in the Al-particle and the Al-substrate, no drastic drop of the instantaneous yield stress, no sudden increase of the equivalent plastic strain or temperature are observed within the velocity range of 50 to 950 m/s.

3.3. Evaluation of the ASI criteria

The ASI criteria defined in Eqs. (4) and (5) is evaluated for Al-on-sapphire (950 m/s) and Al-on-Al impacts (950 m/s). The evolution of the flow stress, σ_Y , strain-rate $\dot{\epsilon}_p$, temperature, T, and rate of change of temperature, \dot{T} , with strain ϵ_p are shown for P1 and P5 in Fig. 14. Note that points P1 and P5 are chosen as they experience the highest level of deformation in Al-on-sapphire and

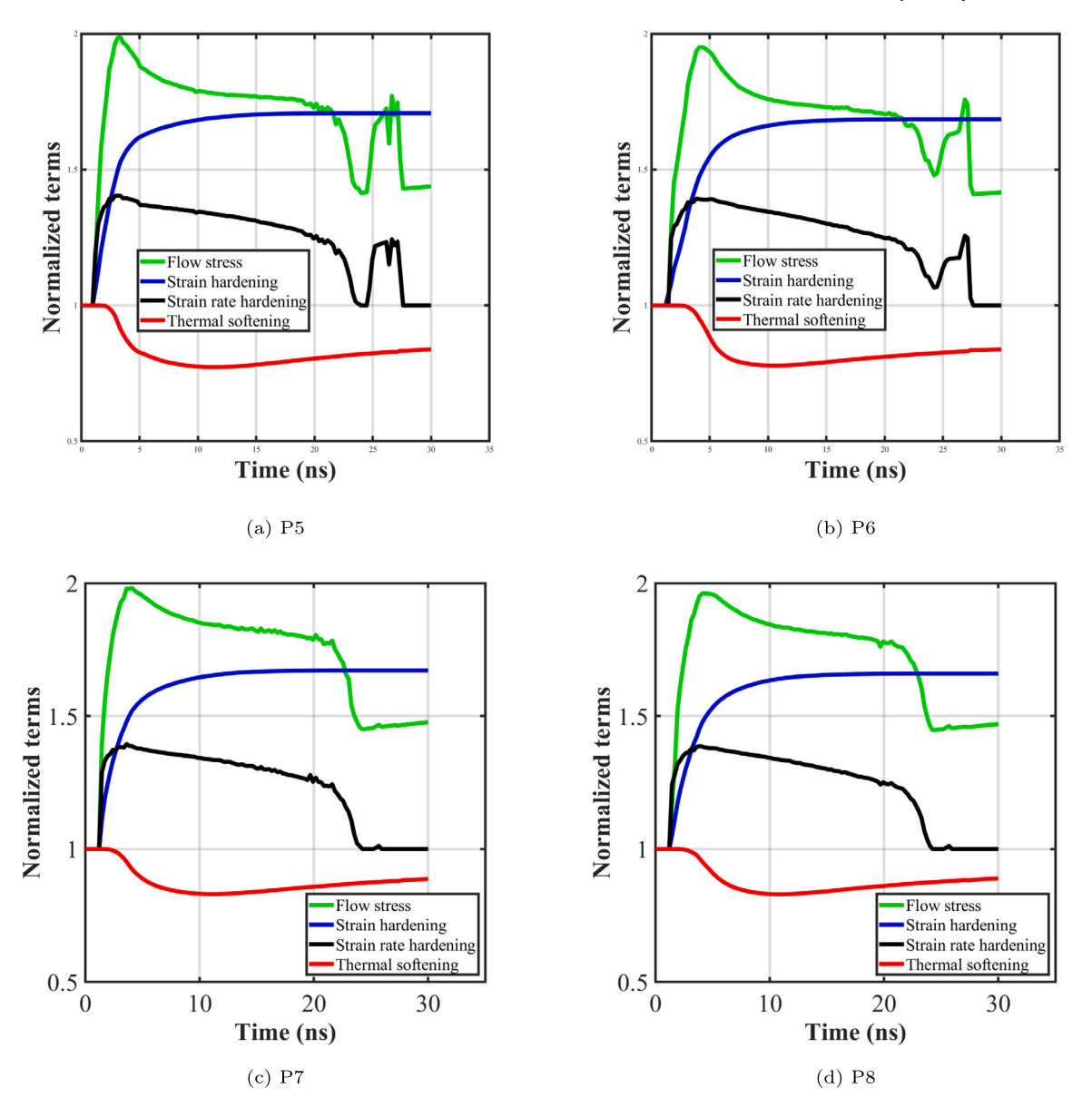


Fig. 12. Evolution of the normalized yield stress ($\bar{\sigma} = \sigma/A$, i.e. yield stress normalized against A) and the each one of the physical terms that contribute to JC-model plotted in the first 30 ns, for Al-on-Al impact at $V_i = 800$ m/s. The four material points with most extreme material behaviors are shown, (a) P5, (b) P6, (c) P7, (d) P8.

Al-on-Al impacts, respectively. Fig. 14(a) shows that at this material point the flow stress starts to drop around an $\varepsilon_p = 0.4$ while the strain rate remains constant. This shows that the material strength is dropping while the material is still being loaded as described by Chen et al. (2018). Therefore, we conclude that the quantitative criterion for ASI is met at material point P1. Recall that Chen et al. similarly predicted adiabatic shear instability at point P1 by inspecting time history of flow stress and temperature (Chen et al., 2018; Chen, 2020). In Al-on-sapphire impacts there are other material points that experience ASI according to the criterion presented in equations Eqs. (4) and (5), but they are not shown here for space considerations. Fig. 14(b) shows the corresponding temperature and rate of change of temperature change at P1. The temperature is on the rise throughout the entire process and remaining well below the melting point of the material. Rate of temperature rise continually increases and reaches up to 140 K/ns at a strain level of 1.5 after which it drops.

For Al-on-Al impacts, the flow stress, strain rate, temperature and rate of change of temperature are plotted as functions of equivalent plastic strain for point P5 in Figs. 14(c) and 14(d). This material point experiences some drop in the flow stress as the plastic strain accumulates. However, the strain rate is always on a decreasing trend when flow stress decreases. Therefore, we conclude that point P5 does not experience adiabatic shear instability, but it is rather being gradually unloaded. This conclusion is

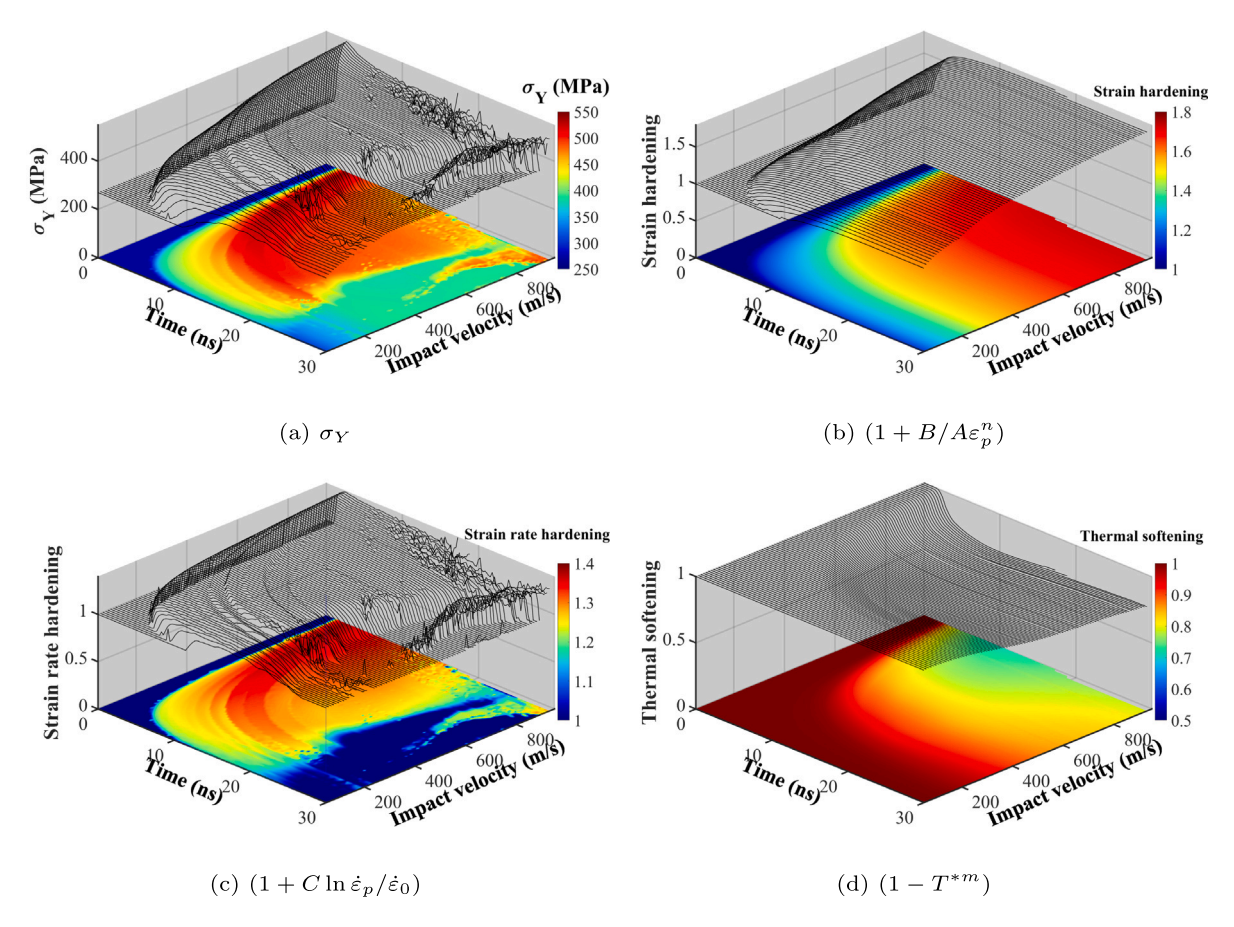


Fig. 13. Flow stress and three terms contributing to JC-model of P5 as functions of time and velocity. (a) flow stress, (b) strain hardening, (c) strain rate hardening, (d) thermal softening. Impact velocities are varied between 50–950 m/s with intervals of 10 m/s.

consistent with the results discussed for Figs. 12 and 13. The temperature at P5 rises to 250 deg. C. And, the rate of temperature increase rise up to 150 K/ns. While this rate is higher than that in Al-on-sapphire impact cases it starts to decrease at an equivalent plastic strain level of 0.5; indicating that the severe loading in the material ends sooner for Al-on-Al impacts. None of the material points in Al-on-Al impacts satisfy the ASI criterion in Eqs. (4) and (5)

3.4. The appropriate material model for UHSR deformations

Material response in high velocity impact of metal particles involves many coupled, physical phenomena. There is general agreement that strain rate in such impacts reaches well into the ultra high strain rate (UHSR) regime. In this regime drag on moving dislocations by phonons or electrons dominate the material behavior (Lesuer et al., 2001) and result in enhanced strain-rate hardening, compared to the regime where thermally activated dislocation motion dominates the strain-rate hardening. Therefore, it is important for the flow stress model to accommodate the extended-hardening in the UHSR regime. The material parameters of the empirical bilinear-JC model presented in Eqs. (1) and (2), have been tuned for high velocity impacts and should respond properly at the UHSR. The linear-JC model does not accommodate UHSR and results in considerably softer material response. Fig. 17 shows a comparison of the flow stress predictions with the linear and bilinear versions of the JC-model against experimental measurements. The flow stress is presented as its ratio against corresponding static yield stress. The experimental measurements are adopted from Manes et al. (2011) and Lesuer et al. (1999). Note that the bilinear JC model values are lower than the experimental results, because the measurements were from Split-Hopkinson Pressure bar test, but the bilinear JC model was calibrated based on Alon-sapphire single particle impacts (Xie et al., 2017; Chen et al., 2018). The material parameters provided in Table 1 for these models are taken from (Lesuer et al., 2001) and Xie et al. (2017), Chen et al. (2018), respectively. This shows that beyond the threshold strain rate the linear-JC model significantly underestimates the flow stress. It has been reported that linear-JC model presents difficulty in accurately predicting particle deformation in Al-on-sapphire impacts (Alizadeh, 2016), particle flattens excessively due to the underestimation of yield stress by linear-JC model.

Here we compare the two approaches by conducting Al-on-Al particle impacts using the JC-model in its bilinear and linear forms. The average strain rate histories during impact are plotted by using both forms of the JC models in Fig. 18, in order to assess the

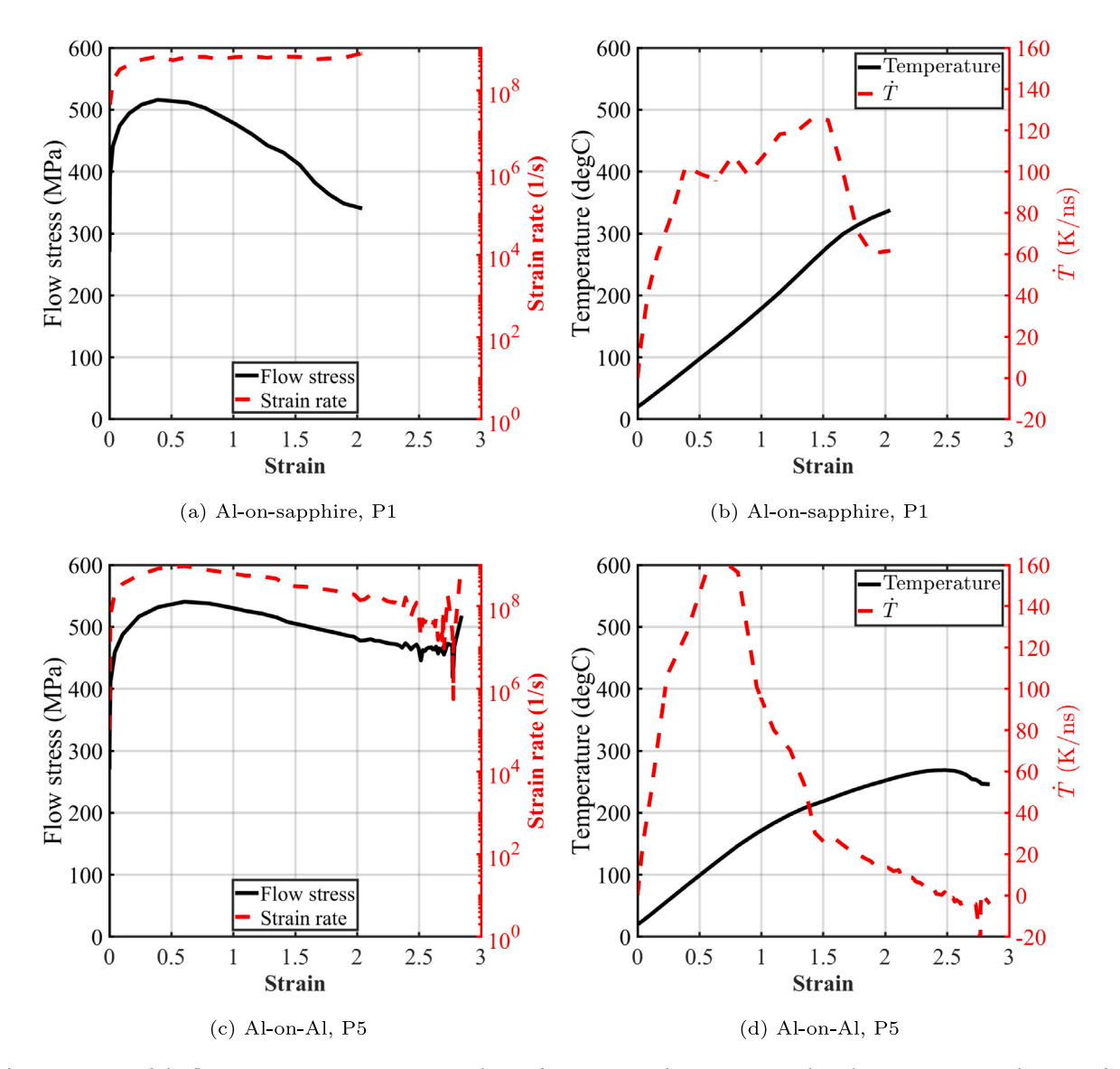


Fig. 14. Variation of the flow stress, strain rate, temperature and rate of temperature with respect to equivalent plastic strain at material point P1 for Al-on-sapphire (for $V_i = 950$ m/s) impact and material point 5 for Al-on-Al impacts with (for $V_i = 950$ m/s).

strain rate variation in the particle. Note that most dynamic action with the high strain rates subside after 30 n/s. The internal wave reflections after bonding are captured in the strain rate regime of 0–597.2 s^{-1} . Both models predict that the largest volume of the material is in the strain rate regime where $\dot{e}_p > 10^7$, during the initial impact period. It is also observed that the particle is compressed more and spreads wider with the linear-JC model as shown in Fig. 19.

The bilinear Johnson–Cook plasticity model was adopted for the analysis presented in the previous sections,. However if the plasticity model is switched back from the bilinear-JC model to the linear-JC model (Lesuer et al., 2001) which generally makes the material behave softer, evidence of a classical adiabatic shear instability (Assadi et al., 2003; Grujicic et al., 2004) can be spotted in several material points inside the particle, especially in the high-shear zone. Fig. 15 shows a comparison of the strain rate history of point P9 for the Al-on-Al impact at 930 m/s.

An obvious jump in temperature around 21 ns is observed for P9 located in the high shear zone as described in Fig. 7(b). At the same time, the flow stress of P9 drastically decreases and plastic strain quickly accumulates. This phenomenon is similar to what Assadi et al. (2003) and Grujicic et al. (2004) have reported in their previous works, defined as adiabatic shear instability. Additionally, the equivalent plastic strain evolution for P9 is shown in Fig. 16. For velocities towards the higher end of the spectrum, i.e. near 900 m/s, the drastic jump of accumulation of plastic strain can be found in the cases with the linear-JC model, while such behavior is not present with the bilinear-JC model, there is

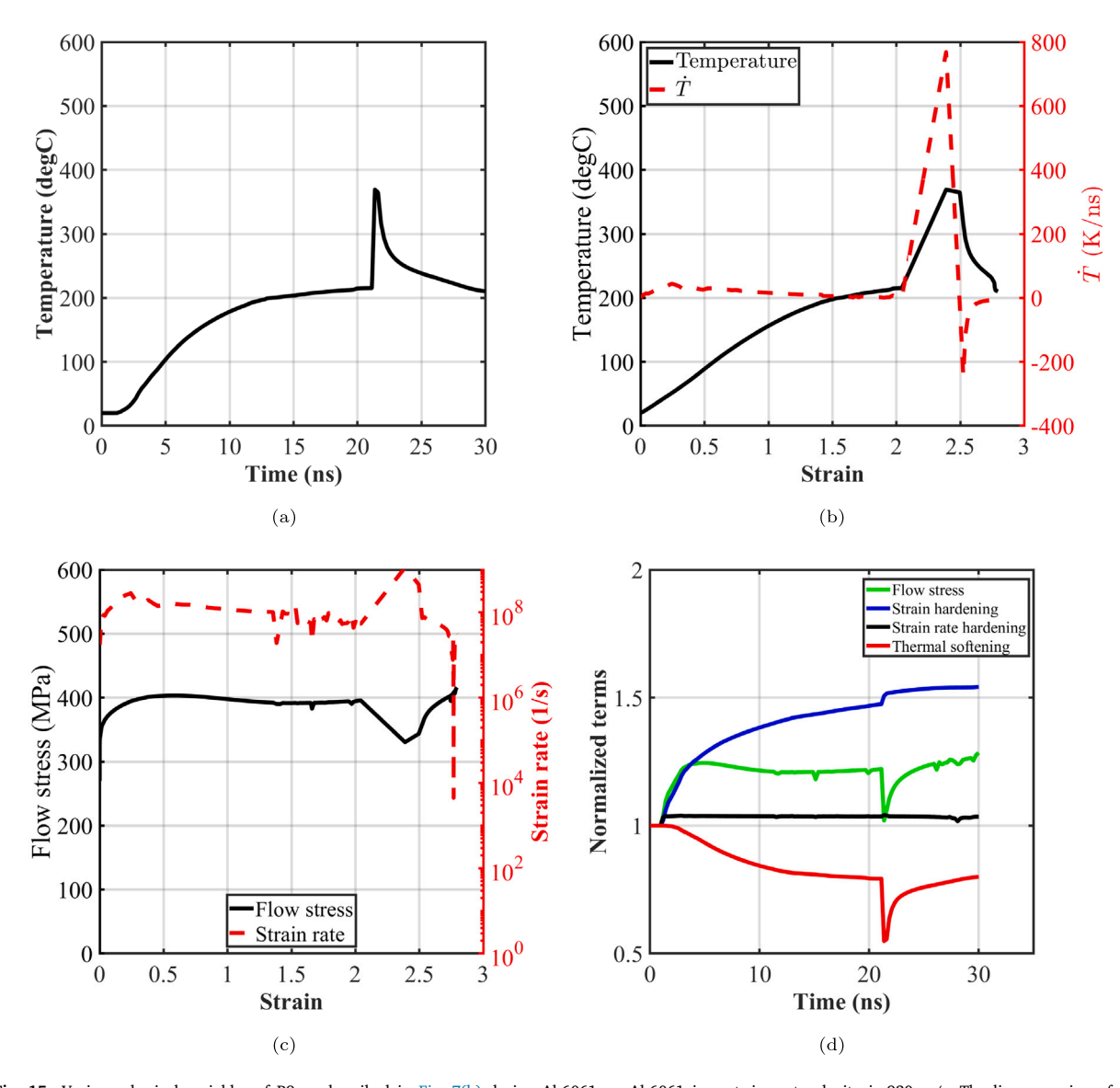


Fig. 15. Various physical variables of P9 as described in Fig. 7(b) during Al-6061 on Al-6061 impact, impact velocity is 930 m/s. The linear version of JC plasticity model was adopted. (a) temperature history, (b) temperature and rate of temperature change and (c) flow stress and strain rate, (d) JC terms values.

no material point in the particle or substrate that demonstrates such behavior. Therefore, the presence of adiabatic shear instability during Al-6061 on Al-6061 impact is possibly an artifact due to the selection of material model. Moreover, with the linear-JC model, excessive element distortion occurs in the elements where material instability is observed, raising further questions about the presence of material instability. More details about post-deformation element quality are provided in Chen (2020).

4. Summary and conclusions

Impact of micron-scale Al-6061 particles on Al-6061 and sapphire substrates is analyzed. Simulation results reveal no evidence of ASI in Al-on-Al impacts unlike the Al-on-sapphire impacts (Chen et al., 2018). This conclusion is further confirmed by using a quantitative ASI criterion and checking each material point in the particle and the substrate. For the Al-on-Al system, using an inappropriate plasticity model leads to excessive element distortion that in turn leads to prediction of ASI as a numerical artifact. While flow stress reduction and localized plastic deformation might be contributing factors to interfacial bonding in the physical world, occurrence of ASI cannot be reliably claimed for this material system.

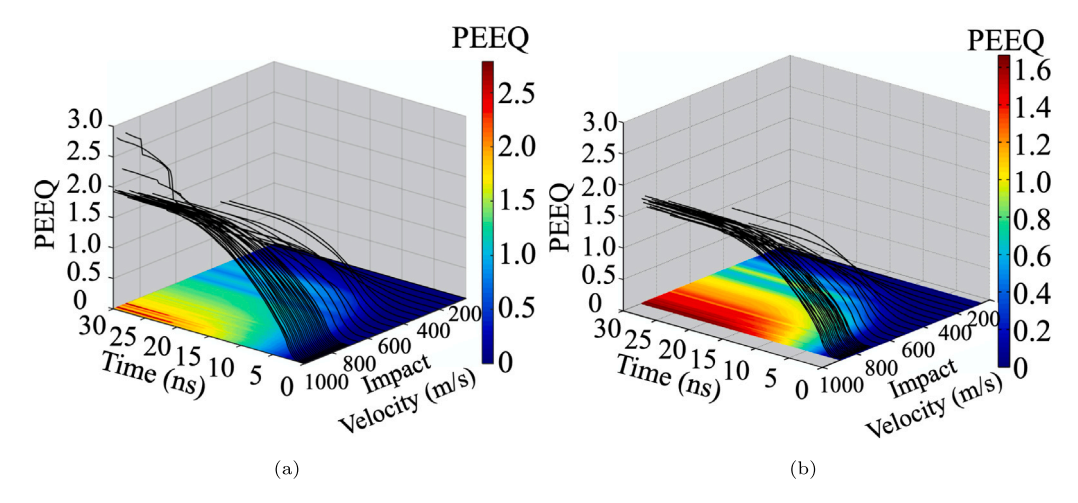


Fig. 16. Evolution of equivalent plastic strain for the entire velocity spectrum for P9 during Al-6061 on Al-6061 impact, (a) with linear-JC model, (b) with bilinear-JC model.

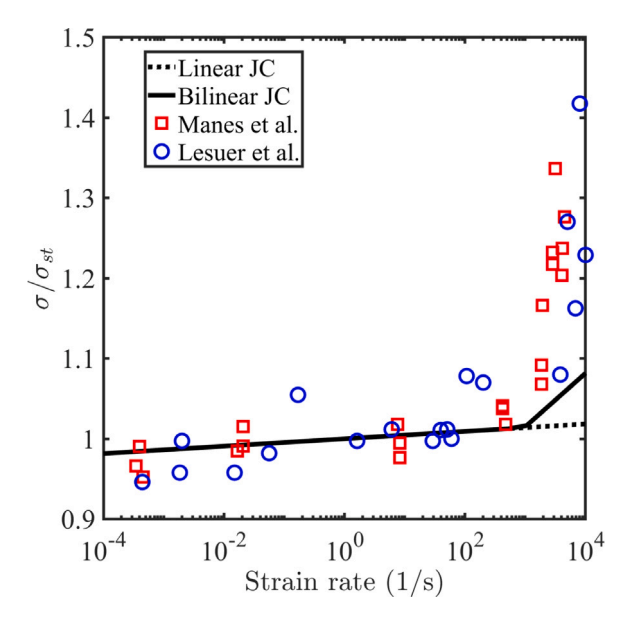


Fig. 17. Comparison of the flow stress predicted by the linear and bilinear Johnson–Cook model as a function of plastic strain rate. Experimental measurements are adapted from Manes et al. (2011) and Lesuer et al. (1999).

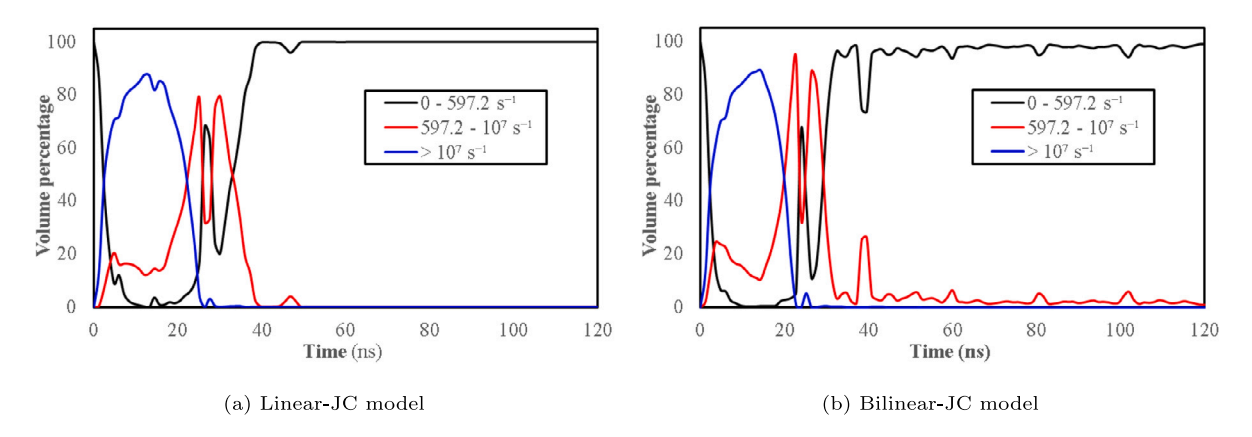


Fig. 18. Volume percentage of various strain rate ranges, variation with time during Al-on-Al impacts at 930 m/s. Computed by using (a) the linear version and (b) the bilinear versions of the JC model.

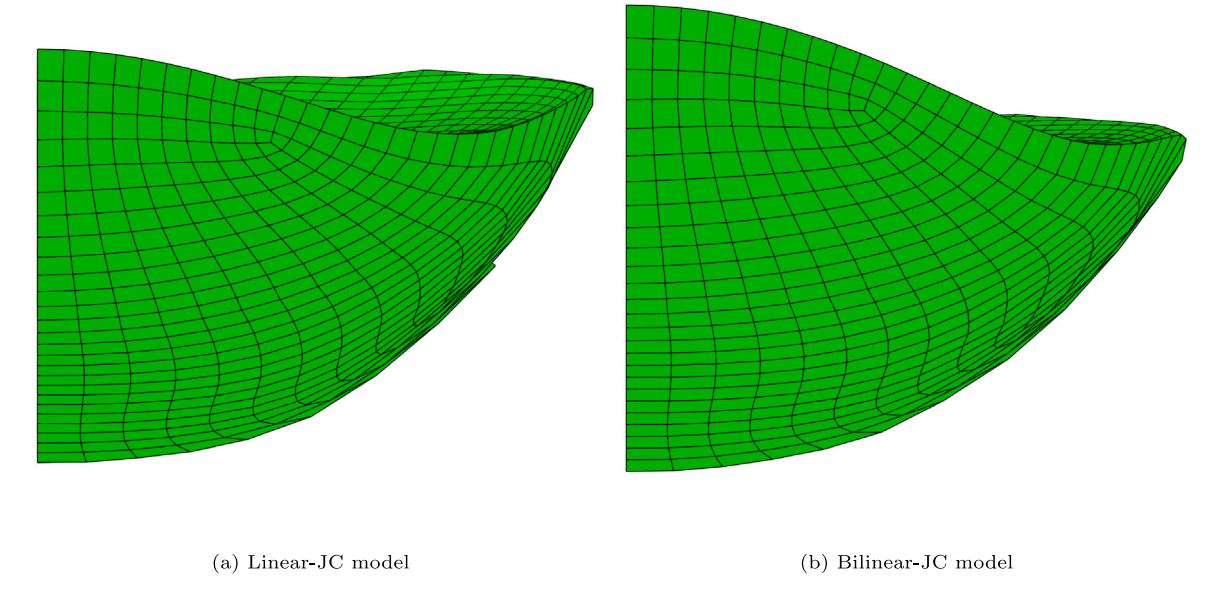


Fig. 19. Comparison of the deformed shapes of the particle computed by using (a) the linear version and (b) the bilinear versions of the JC model, for Al-on-Al impacts at 930 m/s. Linear JC predicts more prominent flattening post-impact.

CRediT authorship contribution statement

Qiyong Chen: Investigation, Conceptualization, Methodology, Writing – original draft, Visualization, Formal analysis. Wanting Xie: Investigation, Conceptualization, Methodology. Victor K. Champagne: Funding acquisition. Aaron Nardi: Writing – review & editing, Funding acquisition. Jae-Hwang Lee: Conceptualization, Methodology, Funding acquisition, Project administration. Sinan Müftü: Conceptualization, Methodology, Formal analysis, Writing – review & editing, Project administration, Funding acquisition.

Declaration of competing interest

The authors declare that they have no known competing financial interests or personal relationships that could have appeared to influence the work reported in this paper.

Data availability

Data will be made available on request.

Acknowledgments

This work was conducted in part through a cooperative research agreement with the US Army Research Laboratory, under contract numbers W911NF-15-2-026 and W911NF-20-2-0024, and a grant from the National Science Foundation (NSF, CMMI-1760924). Any findings, opinions, conclusions or recommendations expressed in this material are those of the authors and do not reflect necessarily the views of the sponsors.

Appendix. Effects of element removal on the results

Elements whose accumulated plastic strain exceeds the limiting strain value (ϵ_f) are removed from analysis as described in Section 2.4. Fig. A.20 shows that up 11% of the mass is removed in Al-on-sapphire impacts due to elements reaching this limiting criterion. Element removal starts near the impact velocity of 500 m/s and reaches its peak around 900 m/s. In Al-on-sapphire impacts ASI is predicted even though elements are removed from analysis. It is reasonable to assume that if the element removal had not been used, more elements could have experienced ASI. But, as stated in Section 2.2, Lagrangian model without element removal results in an unreliable solution.

For Al-on-Al impacts, mass loss due to element removal starts around impact velocity of 900 m/s and remains below 2% at 950 m/s. ASI is not predicted by the model in the entire range of impact velocities (50–950 m/s). Figs. 14,14(c) & 14(d) show the variation of flow stress with plastic strain for point P5. This is the material point that shows the highest level of plastic strain in the particle in Al-on-Al cases. Even though the total accumulated plastic strain is greater than 2.5 no evidence of ASI is seen at this point. However, we cannot exclude the possibility of ASI occurring in the elements that had been removed, had they been allowed to remain in the analysis. Nevertheless, in the velocity range of 0–900 m/s, in which no elements are removed from analysis, ASI is not detected in this computational framework.

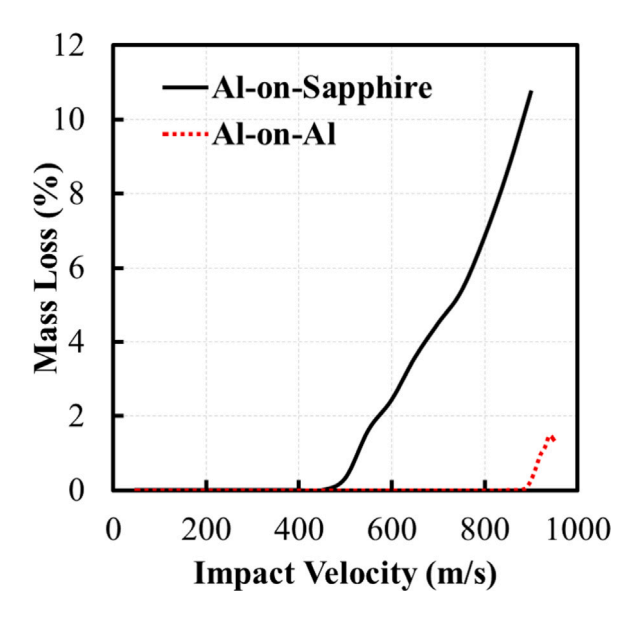


Fig. A.20. Mass loss due to material failure and element removal in Al-on-sapphire and Al-on-Al impact simulations.

References

Al-Juaid, A.A., Othman, R., 2016. Modeling of the strain rate dependency of polycarbonate's yield stress: evaluation of four constitutive equations. J. Eng. 2016. Alizadeh, A., 2016. Tuning Johnson–Cook material model parameters for impact of high velocity, micron scale aluminum particles (Ph.D. thesis). Northeastern University

Anon, 1998. MPDB material property database. URL https://www.jahm.com/pages/about mpdb.html.

Anonymous, 2022. Abaqus/explicit 2022 user manual, dasault system, simulia corp..

Armstrong, R., Zerilli, F., 1994. Dislocation mechanics aspects of plastic instability and shear banding. Mech. Mater. 17 (2-3), 319-327.

Arriaga, M., Waisman, H., 2017. Combined stability analysis of phase-field dynamic fracture and shear band localization. Int. J. Plast. 96, 81-119.

Assadi, H., Gärtner, F., Klassen, T., Kreye, H., 2019. Comment on 'Adiabatic shear instability is not necessary for adhesion in cold spray'. Scr. Mater. 162, 512-514.

Assadi, H., Gartner, F., Stoltenhoff, T., Kreye, H., 2003. Bonding mechanism in cold gas spraying. Acta Mater. 51 (15), 4379-4394.

Bai, Y., 1982. Thermo-plastic instability in simple shear. J. Mech. Phys. Solids 30 (4), 195-207.

Bala, N., Singh, H., Karthikeyan, J., Prakash, S., 2014. Cold spray coating process for corrosion protection: a review. Surf. Eng. 30 (6), 414-421.

Berger-Vergiat, L., Chen, X., Waisman, H., 2019. Explicit and implicit methods for shear band modeling at high strain rates. Comput. Mech. 63 (4), 615–629. Berger-Vergiat, L., Waisman, H., 2017. An overlapping domain decomposition preconditioning method for monolithic solution of shear bands. Comput. Methods Appl. Mech. Engrg. 318, 33–60.

Bhagavathula, K.B., Azar, A., Ouellet, S., Satapathy, S., Dennison, C.R., Hogan, J.D., 2018. High rate compressive behaviour of a dilatant polymeric foam. J. Dyn. Behav. Mater. 4 (4), 573–585.

Bhagavathula, K., Meredith, C., Ouellet, S., Satapathy, S., Romanyk, D., Hogan, J., 2022. Density, microstructure, and strain-rate effects on the compressive response of polyurethane foams. Exp. Mech. 62 (3), 505–519.

Cao, Y., Zhang, D.-d., Liu, J.-x., Liu, K., Du, J.-g., He, W.-b., Ma, J., 2020. The mechanical performance and a rate-dependent constitutive model for Al3Ti compound. Def. Technol. 16 (3), 627–634.

Chakrabarty, R., Song, J., 2020. A modified Johnson-Cook material model with strain gradient plasticity consideration for numerical simulation of cold spray process. Surf. Coat. Technol. 397, 125981.

Champagne, V., Helfritch, D., Leyman, P., Grendahl, S., Klotz, B., 2005. Interface material mixing formed by the deposition of copper on aluminum by means of the cold spray process. J. Therm. Spray Technol. 14 (3), 330–334.

Champagne, V., et al., 2007. The Cold Spray Materials Deposition Process. Elsevier.

Chen, Q., 2020. On the Mechanics and Material-Response of Metal Particles in Cold Spray Impacts (Ph.D. thesis). Northeastern University.

Chen, Q., Alizadeh, A., Xie, W., Wang, X., Champagne, V., Gouldstone, A., Lee, J.-H., Müftü, S., 2018. High-strain-rate material behavior and adiabatic material instability in impact of micron-scale Al-6061 particles. J. Therm. Spray Technol. 27 (4), 641–653.

Chen, L., Edwards, T.E.J., Di Gioacchino, F., Clegg, W.J., Dunne, F.P., Pham, M.-S., 2019. Crystal plasticity analysis of deformation anisotropy of lamellar TiAl alloy: 3D microstructure-based modelling and in-situ micro-compression. Int. J. Plast. 119, 344–360.

Cheng, X., Wang, F., Li, S., Wang, L., 2007. Numerical simulation on the penetrations of long-rod projectiles with different nose shapes. Acta Armamentarii 28 (8), 930–933.

Cheng, X., Wang, F., Li, S., Yuan, S., 2006. Research on novel self-sharpen tungsten alloys.. Rare Met. Mater. Eng. 35 (11), 1761-1764.

Clifton, R., Duffy, J., Hartley, K., Shawki, T., 1984. On Critical Conditions for Shear Band Formation at High Strain Rates. Tech. Rep., Brown Univ Providence Ri Div of Engineering.

Couque, H., Boulanger, R., Bornet, F., 2006. A modified Johnson–Cook model for strain rates ranging from 10³ to 10⁵ s⁻¹. In: J. Physique (Proceedings). 134, 87–93.

Culver, R., 1973. Thermal instability strain in dynamic plastic deformation. In: Metallurgical Effects at High Strain Rates. Springer, pp. 519-530.

dos Santos, T., Srivastava, A., Rodríguez-Martínez, J.A., 2021. The combined effect of size, inertia and porosity on the indentation response of ductile materials. Mech. Mater. 153, 103674.

Edwards, T.E.J., Di Gioacchino, F., Clegg, W.J., 2019a. An experimental study of the polycrystalline plasticity of lamellar titanium aluminide. Int. J. Plast. 118, 291–319.

Edwards, T.E.J., Di Gioacchino, F., Clegg, W.J., 2021. High resolution digital image correlation mapping of strain localization upon room and high temperature, high cycle fatigue of a TiAl intermetallic alloy. Int. J. Fatigue 142, 105905.

Edwards, T.E.J., Di Gioacchino, F., Goodfellow, A.J., Clegg, W.J., 2019b. Slip bands in lamellar TiAl during high cycle fatigue microcompression by correlative total strain mapping, diffraction orientation mapping and transmission electron imaging. Int. J. Fatigue 124, 520–527.

Edwards, T.E.J., Di Gioacchino, F., Muñoz-Moreno, R., Clegg, W.J., 2017. The interaction of borides and longitudinal twinning in polycrystalline TiAl alloys. Acta Mater. 140, 305–316.

El-Qoubaa, Z., Othman, R., 2015. Characterization and modeling of the strain rate sensitivity of polyetheretherketone's compressive yield stress. Mater. Des. (1980-2015) 66, 336-345.

Evans, W., Dan, X., Houshmand, A., Müftü, S., Ando, T., 2019. Microstructural characterization of aluminum 6061 splats cold spray deposited on aluminum 6061-T6 substrate. Metall. Mater. Trans. A 50, 3937–3948.

Fan, X., Zhang, Y., Gao, P., Lei, Z., Zhan, M., 2017. Deformation behavior and microstructure evolution during hot working of a coarse-grained Ti-5Al-5Mo-5V-3Cr-1Zr titanium alloy in beta phase field. Mater. Sci. Eng. A 694, 24–32.

Fardan, A., Berndt, C.C., Ahmed, R., 2021. Numerical modelling of particle impact and residual stresses in cold sprayed coatings: A review. Surf. Coat. Technol. 409, 126835.

Fauchais, P.L., Heberlein, J.V., Boulos, M., 2014. Cold spray. In: Thermal Spray Fundamentals. Springer, pp. 305-382.

Feng, X., Zhang, J., Wang, Y., Hou, Z., Wu, K., Liu, G., Sun, J., 2017. Size effects on the mechanical properties of nanocrystalline NbMoTaW refractory high entropy alloy thin films. Int. J. Plast. 95, 264–277.

Gao, T., Ying, L., Hu, P., Han, X., Rong, H., Wu, Y., Sun, J., 2020. Investigation on mechanical behavior and plastic damage of AA7075 aluminum alloy by thermal small punch test: Experimental trials, numerical analysis. J. Manuf. Process. 50, 1–16.

Gao, C., Zhang, L., 2012. Constitutive modelling of plasticity of fcc metals under extremely high strain rates. Int. J. Plast. 32, 121-133.

Gartner, F., 2006. Advances in cold spraying. Surf. Eng. 22 (3), 161-163. http://dx.doi.org/10.1179/174329406X108906.

Gray, G., 2000. Classic Split-Hopkinson Pressure Bar Testing. ASM International, Materials Park, OH, pp. 462-476.

Grujicic, M., Saylor, J., Beasley, D., DeRosset, W., Helfritch, D., 2003. Computational analysis of the interfacial bonding between feed-powder particles and the substrate in the cold-gas dynamic-spray process. Appl. Surf. Sci. 219 (3), 211–227.

Grujicic, M., Zhao, C., DeRosset, W., Helfritch, D., 2004. Adiabatic shear instability based mechanism for particles/substrate bonding in the cold-gas dynamic-spray process. Mater. Des. 25 (8), 681–688.

Habib, S.A., Khan, A.S., Gnäupel-Herold, T., Lloyd, J.T., Schoenfeld, S.E., 2017. Anisotropy, tension-compression asymmetry and texture evolution of a rare-earth-containing magnesium alloy sheet, ZEK100, at different strain rates and temperatures: Experiments and modeling. Int. J. Plast. 95, 163–190.

Habib, S.A., Lloyd, J.T., Meredith, C.S., Khan, A.S., Schoenfeld, S.E., 2019. Fracture of an anisotropic rare-earth-containing magnesium alloy (ZEK100) at different stress states and strain rates: Experiments and modeling. Int. J. Plast. 122, 285–318.

Habib, S.A., Meredith, C.S., Khan, A.S., 2021. Quasi-static and dynamic investigation of an advanced high strength and corrosion resistant 10% Cr nanocomposite martensitic steel. Int. J. Mech. Sci. 211, 106774.

Harding, J., Wood, E., Campbell, J., 1960. Tensile testing of materials at impact rates of strain. J. Mech. Eng. Sci. 2 (2), 88-96.

Hassani-Gangaraj, M., Veysset, D., Champagne, V., Nelson, K., Schuh, C., 2018. Adiabatic shear instability is not necessary for adhesion in cold spray. Acta Mater. 158, 430-439.

Hassani-Gangaraj, M., Veysset, D., Champagne, V.K., Nelson, K.A., Schuh, C.A., 2019. Response to comment on "Adiabatic shear instability is not necessary for adhesion in cold spray". Scr. Mater. 162, 515–519.

Hauser, F., 1966. Techniques for measuring stress-strain relations at high strain rates. Exp. Mech. 6 (8), 395-402.

Horn, T.D., Silbermann, C.B., Frint, P., Wagner, M.F.-X., Ihlemann, J., 2018. Strain localization during equal-channel angular pressing analyzed by finite element simulations. Metals 8 (1), 55.

Hu, P., Ying, L., He, B., 2017. Hot Stamping Advanced Manufacturing Technology of Lightweight Car Body. Springer.

Huang, S., Feng, X., Xia, K., 2011. A dynamic punch method to quantify the dynamic shear strength of brittle solids. Rev. Sci. Instrum. 82 (5), 053901.

Huang, Y., Ning, Z., Shen, Z., Liang, W., Sun, H., Sun, J., 2017. Bending behavior of as-cast and annealed ZrCuNiAl bulk metallic glass. J. Mater. Sci. Technol. 33 (10), 1153–1158.

Huh, H., Kang, W., 2002. Crash-worthiness assessment of thin-walled structures with the high-strength steel sheet. Int. J. Veh. Des. 30 (1-2), 1-21.

Iftikhar, C.M.A., Li, Y.L., Kohar, C.P., Inal, K., Khan, A.S., 2021. Evolution of subsequent yield surfaces with plastic deformation along proportional and non-proportional loading paths on annealed AA6061 alloy: Experiments and crystal plasticity finite element modeling. Int. J. Plast. 143, 102956.

Im, S., Chen, Z., Johnson, J.M., Zhao, P., Yoo, G.H., Park, E.S., Wang, Y., Muller, D.A., Hwang, J., 2018. Direct determination of structural heterogeneity in metallic glasses using four-dimensional scanning transmission electron microscopy. Ultramicroscopy 195, 189–193.

Im, S., Wang, Y., Zhao, P., Yoo, G.H., Chen, Z., Calderon, G., Gharacheh, M.A., Zhu, M., Licata, O., Mazumder, B., et al., 2021. Medium-range ordering, structural heterogeneity, and their influence on properties of Zr-Cu-Co-Al metallic glasses. Phys. Rev. Mater. 5 (11), 115604.

Im, S., Zhao, P., Yoo, G.H., Chen, Z., Calderon, G., Gharacheh, M.A., Licata, O., Mazumder, B., Muller, D.A., Park, E.S., et al., 2020. Structural heterogeneity, ductility, and glass forming ability of Zr-based metallic glasses. arXiv preprint arXiv:2002.09347.

Intrater, J., 2002. Cold spray technology - Prospects and applications. Surf. Eng. 18 (5), 321-323.

Jacques, N., Rodríguez-Martínez, J., 2021. Influence on strain-rate history effects on the development of necking instabilities under dynamic loading conditions. Int. J. Solids Struct. 230, 111152.

Jaspers, S., Dautzenberg, J., 2002. Material behaviour in conditions similar to metal cutting: flow stress in the primary shear zone. J. Mater Process. Technol. 122 (2–3), 322–330.

Jiang, S., Guo, S., Huang, Y., Ning, Z., Xue, P., Ru, W., Zhang, J., Sun, J., 2019. In situ study of the shear band features of a CuZr-based bulk metallic glass composite. Intermetallics 112, 106523.

Jiang, S.-S., Huang, Y.-J., Wu, F.-F., Xue, P., Sun, J.-F., 2018. A CuZr-based bulk metallic glass composite with excellent mechanical properties by optimizing microstructure. J. Non-Cryst. Solids 483, 94–98.

Johnson, G., Cook, W., 1983. A constitutive model and data for metals subjected to large strains, high strain rates and high temperatures. In: Proceedings of the 7th International Symposium on Ballistics, Vol. 21. The Hague, The Netherlands, pp. 541–547.

Johnson, G., Cook, W., 1985. Fracture characteristics of three metals subjected to various strains, strain rates, temperatures and pressures. Eng. Fract. Mech. 21 (1), 31–48.

Kabirian, F., Khan, A.S., Pandey, A., 2014. Negative to positive strain rate sensitivity in 5xxx series aluminum alloys: Experiment and constitutive modeling. Int. J. Plast. 55, 232–246.

Kapan, E., Shafaghi, N., Ucar, S., Aydıner, C.C., 2017. Texture-dependent character of strain heterogeneity in magnesium AZ31 under reversed loading. Mater. Sci. Eng. A 684, 706–711.

Keeler, S., Backofen, W., 1963. Plastic instability and fracture in sheets stretched over rigid punches. Asm Trans. Q. 56 (1), 25-48.

Khan, A., Liang, R., 1999. Behaviors of three BCC metal over a wide range of strain rates and temperatures: experiments and modeling. Int. J. Plast. 15 (10), 1089–1109.

Khan, A., Liang, R., 2000. Behaviors of three BCC metals during non-proportional multi-axial loadings: experiments and modeling. Int. J. Plast. 16 (12), 1443–1458.

Khosravani, A., Thadhani, N., Kalidindi, S.R., 2021. Microstructure quantification and multiresolution mechanical characterization of Ti-based bulk metallic glass-matrix composites. Jom 73 (11), 3312–3322.

Klinkov, S., Kosarev, V., Rein, M., 2005. Cold spray deposition: Significance of particle impact phenomena. Aerosp. Sci. Technol. 9 (7), 582–591. http://dx.doi.org/10.1016/j.ast.2005.03.005.

Kolsky, H., 1949. An investigation of the mechanical properties of materials at very high rates of loading. Proc. Phys. Soc. Sect. B 62 (11), 676.

Ku, A., 2020. Thermo-mechanical response, anisotropy, and texture evolution of two overaged Al 7056 alloy plates in T761 and T721 tempers: Experiments and modeling. UMBC Stud. Collect.

Ku, A.Y., Khan, A.S., Gnäupel-Herold, T., 2020. Quasi-static and dynamic response, and texture evolution of two overaged Al 7056 alloy plates in T761 and T721 tempers: Experiments and modeling. Int. J. Plast. 130, 102679.

Lee, J.-H., Loya, P., Lou, J., Thomas, E., 2014. Dynamic mechanical behavior of multilayer graphene via supersonic projectile penetration. Science 346 (6213), 1092–1096.

Lee, J.-H., Veysset, D., Singer, J., Retsch, M., Saini, G., Pezeril, T., Nelson, K., Thomas, E., 2012. High strain rate deformation of layered nanocomposites. Nature Commun. 3. 1164.

Lemiale, V., King, P., Rudman, M., Prakash, M., Cleary, P., Jahedi, M., Gulizia, S., 2014. Temperature and strain rate effects in cold spray investigated by smoothed particle hydrodynamics. Surf. Coat. Technol. 254, 121–130.

Lesuer, D., Kay, G., LeBlanc, M., 1999. Modeling large strain, high rate deformation in metals. Eng. Res. Dev. Technol.

Lesuer, D.R., Kay, G., LeBlanc, M., 2001. Modeling Large-Strain, High-Rate Deformation in Metals. Tech. Rep., Lawrence Livermore National Lab.(LLNL), Livermore, CA (United States).

Li, Q., 2001. Strain energy density failure criterion. Int. J. Solids Struct. 38 (38-39), 6997-7013.

Li, H.-w., Yan, S.-l., Zhan, M., Zhang, X., 2019. Eddy current induced dynamic deformation behaviors of aluminum alloy during EMF: Modeling and quantitative characterization. J. Mater Process. Technol. 263, 423–439.

Li, Y., Yu, L., Zheng, J.-h., Guan, B., Zheng, K., 2021. A physical-based unified constitutive model of AA7075 for a novel hot forming condition with pre-cooling. J. Alloys Compd. 876, 160142.

Li, Z., Zhan, M., Fan, X., Tan, J., 2017. A modified Johnson-Cook model of as-quenched AA2219 considering negative to positive strain rate sensitivities over a wide temperature range. Procedia Eng. 207, 155-160.

Lin, E., Chen, Q., Ozdemir, O., Champagne, V., Müftü, S., 2019. Effects of interface bonding on the residual stresses in cold-sprayed Al-6061: A numerical investigation. J. Therm. Spray Technol. 28 (3), 472–483.

Lindholm, U., Yeakley, L., 1968. High strain-rate testing: tension and compression. Exp. Mech. 8 (1), 1-9.

Liu, J., He, Y., Xia, M., Hu, Y., 2022. Ultrahigh strain rate-activated superplastic forming of aluminum and gold nanometals. Mater. Des. 221, 110910.

Liu, X.-F., Tian, Z.-L., Zhang, X.-F., Chen, H.-H., Liu, T.-W., Chen, Y., Wang, Y.-J., Dai, L.-H., 2020. "Self-sharpening" tungsten high-entropy alloy. Acta Mater. 186, 257–266.

Lu, Y., Huang, Y., Wu, J., 2018. Laser additive manufacturing of structural-graded bulk metallic glass. J. Alloys Compd. 766, 506-510.

Lu, Y., Su, S., Zhang, S., Huang, Y., Qin, Z., Lu, X., Chen, W., 2021. Controllable additive manufacturing of gradient bulk metallic glass composite with high strength and tensile ductility. Acta Mater. 206, 116632.

Mahadevan, K., Liang, P., Fekete, J., 2000. Effect of strain rate in full vehicle frontal crash analysis. SAE Trans. 863-871.

Manes, A., Lumassi, D., Giudici, L., Giglio, M., 2013. An experimental–numerical investigation on aluminium tubes subjected to ballistic impact with soft core 7.62 ball projectiles. Thin-Walled Struct. 73, 68–80.

Manes, A., Peroni, L., Scapin, M., Giglio, M., 2011. Analysis of strain rate behavior of an Al 6061 T6 alloy. Procedia Eng. 10, 3477-3482.

Marciniak, Z., Kuczyński, K., 1967. Limit strains in the processes of stretch-forming sheet metal. Int. J. Mech. Sci. 9 (9), 609IN1613-612IN2620.

Marvi-Mashhadi, M., Vaz-Romero, A., Sket, F., Rodríguez-Martínez, J., 2021. Finite element analysis to determine the role of porosity in dynamic localization and fragmentation: application to porous microstructures obtained from additively manufactured materials. Int. J. Plast. 143, 102999.

Maurel-Pantel, A., Fontaine, M., Thibaud, S., Gelin, J.-C., 2012. 3D FEM simulations of shoulder milling operations on a 304L stainless steel. Simul. Model. Pract. Theory 22, 13–27.

Meng, M., Fan, X., Guo, L., Zhan, M., 2018. Achieving fine-grained equiaxed alpha via thermo-mechanical loading under off-equilibrium state in two-phase Ti-alloys. J. Mater Process. Technol. 259, 397–408.

Meredith, C.S., 2021. Dynamic thermomechanical behavior of fine-grained Mg alloy AMX602. Materialia 16, 101096.

Meyers, M., 1994. Dynamic Behavior of Materials. John wiley & sons.

Molinari, A., 1985. Thermoviscoplastic instability in simple shear. J. Mec. Theor. Appl. 4 (5), 659-684.

Moridi, A., 2017. Modeling cold spray. In: Powder Consolidation using Cold Spray. Springer, pp. 33-75.

Moridi, A., Hassani-Gangaraj, M., Guagliano, M., Dao, M., 2014. Cold spray coating: review of material systems and future perspectives. Surf. Eng. 30 (6), 369–395.

Munro, M., 1997. Evaluated material properties for a sintered alpha-alumina. J. Am. Ceram. Soc. 80 (8), 1919-1928.

Needleman, A., 1990. An analysis of tensile decohesion along an interface. J. Mech. Phys. Solids 38 (3), 289-324.

N'souglo, K.E., Jacques, N., Rodríguez-Martínez, J.A., 2021. A three-pronged approach to predict the effect of plastic orthotropy on the formability of thin sheets subjected to dynamic biaxial stretching. J. Mech. Phys. Solids 146, 104189.

N'souglo, K.E., Srivastava, A., Osovski, S., Rodríguez-Martínez, J.A., 2018. Random distributions of initial porosity trigger regular necking patterns at high strain rates. Proc. R. Soc. Lond. Ser. A Math. Phys. Eng. Sci. 474 (2211), 20170575.

Othman, R., 2015. A modified eyring equation for modeling yield and flow stresses of metals at strain rates ranging from 10^{-5} to 5×10^4 s⁻¹. Adv. Mater. Sci. Eng. 2015.

Özdür, N.A., Aydıner, C., 2022. Advance of collaborative twinning fields in magnesium AZ31 via the strain and residual intensity channels in microscopic image correlation. In: Challenges in Mechanics of Time Dependent Materials, Mechanics of Biological Systems and Materials & Micro-and Nanomechanics, Volume 2. Springer, pp. 1–9.

Özdür, N., Üçel, I., Yang, J., Aydıner, C., 2021. Residual intensity as a morphological identifier of twinning fields in microscopic image correlation. Exp. Mech. 61 (3), 499–514.

Papyrin, A., Blose, R., 2003. Cold spray technology: From R and D to commercial applications. Mater. Technol. 18 (2), 73-78.

Papyrin, A., Kosarev, V., Klinkov, S., Alkhimov, A., Fomin, V., 2006. Cold Spray Technology. Elsevier.

Pascon, J.P., Waisman, H., 2021a. A mixed finite element formulation for ductile damage modeling of thermoviscoplastic metals accounting for void shearing. Comput. Mech. 67 (5), 1307–1330.

Pascon, J.P., Waisman, H., 2021b. A thermodynamic framework to predict ductile damage in thermoviscoplastic porous metals. Mech. Mater. 153, 103701.

Preston, D., Tonks, D., Wallace, D., 2003. Model of plastic deformation for extreme loading conditions. J. Appl. Phys. 93 (1), 211-220.

Recht, R.F., 1964. Catastrophic thermoplastic shear. J. Appl. Mech. 31 (2), 189-193. http://dx.doi.org/10.1115/1.3629585.

Rittel, D., Lee, S., Ravichandran, G., 2002. A shear-compression specimen for large strain testing. Exp. Mech. 42 (1), 58-64.

Rodríguez-Martínez, J.A., Molinari, A., Zaera, R., Vadillo, G., Fernández-Sáez, J., 2017. The critical neck spacing in ductile plates subjected to dynamic biaxial loading: on the interplay between loading path and inertia effects. Int. J. Solids Struct. 108, 74–84.

Roessig, K., Mason, J., 1999. Adiabatic shear localization in the dynamic punch test, part II: numerical simulations. Int. J. Plast. 15 (3), 263-283.

Rong, H., Hu, P., Ying, L., Hou, W., Zhang, J., 2019. Thermal forming limit diagram (TFLD) of AA7075 aluminum alloy based on a modified continuum damage model: Experimental and theoretical investigations. Int. J. Mech. Sci. 156, 59–73.

Rousselier, G., 2021. Porous plasticity revisited: Macroscopic and multiscale modeling. Int. J. Plast. 136, 102881.

Rousselier, G., 2022. Lode-dependent second porosity in porous plasticity for shear-dominated loadings. Int. J. Plast. 159, 103446.

Rousselier, G., Morgeneyer, T.F., Ren, S., Mazière, M., Forest, S., 2017. Interaction of the Portevin-Le Chatelier phenomenon with ductile fracture of a thin aluminum CT specimen: experiments and simulations. Int. J. Fract. 206 (1), 95–122.

Schmidt, T., Assadi, H., Gartner, F., Richter, H., Stoltenhoff, T., Kreye, H., Klassen, T., 2009. From particle acceleration to impact and bonding in cold spraying. J. Therm. Spray Technol. 18 (5–6), 794.

Shafaghi, N., Kapan, E., Aydıner, C., 2020. Cyclic strain heterogeneity and damage formation in rolled magnesium via in situ microscopic image correlation. Exp. Mech. 60 (6), 735–751.

Sun, H., Ning, Z., Ren, J., Liang, W., Huang, Y., Sun, J., Xue, X., Wang, G., 2019. Serration and shear avalanches in a ZrCu based bulk metallic glass composite in different loading methods. J. Mater. Sci. Technol. 35 (9), 2079–2085.

Suresh, S., Lee, S.-W., Aindow, M., Brody, H.D., Champagne, V.K., Dongare, A.M., 2020. Mesoscale modeling of jet initiation behavior and microstructural evolution during cold spray single particle impact. Acta Mater. 182, 197–206.

Svolos, L., Bronkhorst, C.A., Waisman, H., 2020. Thermal-conductivity degradation across cracks in coupled thermo-mechanical systems modeled by the phase-field fracture method. J. Mech. Phys. Solids 137, 103861.

Svolos, L., Mourad, H.M., Bronkhorst, C.A., Waisman, H., 2021. Anisotropic thermal-conductivity degradation in the phase-field method accounting for crack directionality. Eng. Fract. Mech. 245, 107554.

Tuazon, B.J., Bae, K.-O., Lee, S.-H., Shin, H.-S., 2014. Integration of a new data acquisition/processing scheme in SHPB test and characterization of the dynamic material properties of high-strength steels using the optional form of Johnson-Cook model. J. Mech. Sci. Technol. 28 (9), 3561–3568.

Üçel, İ.B., Kapan, E., Türkoğlu, O., Aydıner, C.C., 2019. İn situ investigation of strain heterogeneity and microstructural shear bands in rolled magnesium AZ31. Int. J. Plast. 118, 233–251.

Umbrello, D., M'saoubi, R., Outeiro, J., 2007. The influence of Johnson-Cook material constants on finite element simulation of machining of AISI 316L steel. Int. J. Mach. Tools Manuf. 47 (3-4), 462-470.

Van Steenkiste, T.H., Smith, J.R., Teets, R.E., Moleski, J.J., Gorkiewicz, D.W., Tison, R.P., Marantz, D.R., Kowalsky, K.A., Riggs, II, W.L., Zajchowski, P.H., Pilsner, B., McCune, R.C., Barnett, K.J., 1999. Kinetic spray coatings. Surf. Coat. Technol. 111 (1), 62–71. http://dx.doi.org/10.1016/S0257-8972(98)00709-9.
 Vaz-Romero, A., Rodríguez-Martínez, J.A., Mercier, S., Molinari, A., 2017. Multiple necking pattern in nonlinear elastic bars subjected to dynamic stretching: The role of defects and inertia. Int. J. Solids Struct. 125, 232–243.

Villafuerte, J., 2005. Cold spray: A new technology. Weld. J. (Miami, Fla) 84 (5), 24-29.

Vishnu, A., Marvi-Mashhadi, M., Nieto-Fuentes, J., Rodríguez-Martínez, J., 2022a. New insights into the role of porous microstructure on dynamic shear localization. Int. J. Plast. 148, 103150.

Vishnu, A., Nieto-Fuentes, J.C., Rodríguez-Martínez, J.A., 2022b. Shear band formation in porous thin-walled tubes subjected to dynamic torsion. Int. J. Solids Struct. 252, 111837.

Voyiadjis, G., Abed, F., 2005. Microstructural based models for BCC and FCC metals with temperature and strain rate dependency. Mech. Mater. 37 (2), 355–378. Wright, T.W., Batra, R.C., 1985. The initiation and growth of adiabatic shear bands. Int. J. Plast. 1 (3), 205–212.

Xiao, H., Fan, X., Zhan, M., Liu, B., Zhang, Z., 2021. Flow stress correction for hot compression of titanium alloys considering temperature gradient induced heterogeneous deformation. J. Mater Process. Technol. 288, 116868.

Xie, W., Alizadeh, A., Chen, Q., Champagne, V., Wang, X., Nardi, A.T., Kooi, S., Müftü, S., Lee, J.-H., 2017. Dynamics and extreme plasticity of metallic microparticles in supersonic collisions. Sci. Rep. 7, http://dx.doi.org/10.1038/s41598-017-05104-7, URL https://www.nature.com/articles/s41598-017-05104-7#article-info.

Xue, P., Huang, Y., Pauly, S., Guo, F., Ren, Y., Jiang, S., Guo, F., Guo, S., Fan, H., Ning, Z., et al., 2021. Structural evolution of a CuZr-based bulk metallic glass composite during cryogenic treatment observed by in-situ high-energy X-ray diffraction. J. Alloys Compd. 871, 159570.

Xue, P., Pauly, S., Gan, W., Jiang, S., Fan, H., Ning, Z., Huang, Y., Sun, J., 2019. Enhanced tensile plasticity of a cuzr-based bulk metallic glass composite induced by ion irradiation. J. Mater. Sci. Technol. 35 (10), 2221–2226.

Yan, N., Li, Z., Xu, Y., Meyers, M.A., 2021. Shear localization in metallic materials at high strain rates. Prog. Mater. Sci. 119, 100755.

Ye, G., Jiang, M., Xue, S., Ma, W., Dai, L., 2018. On the instability of chip flow in high-speed machining. Mech. Mater. 116, 104-119.

Ye, G., Xue, S., 2019. Thermal gradient and its contribution to size effect of specific cutting energy. Int. J. Adv. Manuf. Technol. 101 (9), 2327-2339.

Ye, G., Xue, S., Ma, W., Dai, L., 2017. Onset and evolution of discontinuously segmented chip flow in ultra-high-speed cutting Ti-6Al-4V. Int. J. Adv. Manuf. Technol. 88 (1), 1161–1174.

Yildirim, B., 2013. Mechanistic modeling of high velocity micro-particle impacts: Application to material deposition by cold spray process (Ph.D. thesis). Northeastern University.

Yildirim, B., Fukanuma, H., Ando, T., Gouldstone, A., Müftü, S., 2015. A numerical investigation into cold spray bonding processes. J. Tribol. 137 (1), 011102. Yıldırım, B., Hulton, A., Alavian, S.A., Ando, T., Gouldstone, A., Müftü, S., 2012. On simulation of multi-particle impact interactions in the cold spray process. In: International Joint Tribology Conference, Vol. 45080. American Society of Mechanical Engineers, pp. 83–85.

Yildirim, B., Müftü, S., Gouldstone, A., 2011a. Modeling of high velocity impact of spherical particles. Wear 270 (9–10), 703–713.

Yildirim, B., Müftü, S., Gouldstone, A., 2011b. On cohesion of micron scale metal particles in high velocity impact with a metal substrate. In: ASME/STLE 2011 International Joint Tribology Conference. American Society of Mechanical Engineers, pp. 373–375.

Yildirim, B., Yang, H., Gouldstone, A., Müftü, S., 2017. Rebound mechanics of micrometre-scale, spherical particles in high-velocity impacts. Proc. R. Soc. Lond. Ser. A Math. Phys. Eng. Sci. 473 (2204), http://dx.doi.org/10.1098/rspa.2016.0936.

Ying, L., Gao, T., Dai, M., Hu, P., Dai, J., 2021. Towards joinability of thermal self-piercing riveting for AA7075-T6 aluminum alloy sheets under quasi-static loading conditions. Int. J. Mech. Sci. 189, 105978.

Ying, L., Gao, T., Rong, H., Han, X., Hu, P., Hou, W., 2019. On the thermal forming limit diagram (TFLD) with GTN mesoscopic damage model for AA7075 aluminum alloy: Numerical and experimental investigation. J. Alloys Compd. 802, 675–693.

YL, B., Dodd, B., et al., 1992. Adiabatic Shear Localization: Occurrence, Theories, and Applications. Pergamon Press.

You, T., Waisman, H., Chen, W.-Z., Shao, J.-F., Zhu, Q.-Z., 2021. A novel micromechanics-enhanced phase-field model for frictional damage and fracture of quasi-brittle geomaterials. Comput. Methods Appl. Mech. Engrg. 385, 114060.

Zener, C., Hollomon, J.H., 1944. Effect of strain rate upon plastic flow of steel. J. Appl. Phys. 15 (1), 22-32.

Zeng, X., Fan, X., Li, H., Zhan, M., Li, S., 2019. Grain morphology related microstructural developments in bulk deformation of 2219 aluminum alloy sheet at elevated temperature. Mater. Sci. Eng. A 760, 328–338.

Zeng, X., Fan, X., Li, H., Zhan, M., Li, S., Ren, T., Wu, K., 2020. Grain refinement in hot working of 2219 aluminium alloy: On the effect of deformation mode and loading path. Mater. Sci. Eng. A 794, 139905.

Zhao, J., 2011. An overview of some recent progress in rock dynamics research. In: Advances in Rock Dynamics and Applications. CRC Press, USA, pp. 5-33.

Zhao, P., Li, J., Hwang, J., Wang, Y., 2017. Influence of nanoscale structural heterogeneity on shear banding in metallic glasses. Acta Mater. 134, 104-115.

Zhao, J., Li, H., Zhao, Y., 1998. Dynamic Strength Tests of the Bukit Timah Granite. Nanyang Technological University, Singapore.

Zuanetti, B., Ramos, K.J., Cady, C.M., Meredith, C.S., Casem, D.T., Golder, A., Bolme, C.A., 2022. Miniature beryllium split-Hopkinson pressure bars for extending the range of achievable strain-rates. Metals 12 (11), 1834.